Wittmann, H., von Blanckenburg, F., Dannhaus, N., Bouchez, J., Gaillardet, J., Guyot, J., Maurice, L., Roig, H., Filizola, N., Christl, M. (2015): A test of the cosmogenic 10Be(meteoric)/9Be proxy for simultaneously determining basin-wide erosion rates, denudation rates, and the degree of weathering in the Amazon basin. - *Journal of Geophysical Research*, *120*, 12, pp. 2498–2528.

DOI: http://doi.org/10.1002/2015JF003581

AGU PUBLICATIONS

JGR

Journal of Geophysical Research: Earth Surface

RESEARCH ARTICLE
10.1002/2015JF003581

Key Points:
- $^{10}Be/^{9}Be$ ratios in sediment and river water provide weathering and erosion rates in the Amazon
- Meteoric denudation rates agree within a factor of 2 with published in situ rates
- Basin-wide Be weathering intensity is approximately 40% with no floodplain weathering resolvable

Supporting Information:
- Texts S1–S6, Figures S1–S4, and Tables S1–S4

Correspondence to:
H. Wittmann,
wittmann@gfz-potsdam.de

Citation:
Wittmann, H., F. von Blanckenburg, N. Dannhaus, J. Bouchez, J. Gaillardet, J. L. Guyot, L. Maurice, H. Roig, N. Filizola, and M. Christl (2015), A test of the cosmogenic $^{10}Be(meteoric)/^{9}Be$ proxy for simultaneously determining basin-wide erosion rates, denudation rates, and the degree of weathering in the Amazon basin, *J. Geophys. Res. Earth Surf.*, *120*, 2498–2528, doi:10.1002/2015JF003581.

Received 10 APR 2015
Accepted 18 OCT 2015
Accepted article online 22 OCT 2015
Published online 14 DEC 2015

A test of the cosmogenic $^{10}Be(meteoric)/^{9}Be$ proxy for simultaneously determining basin-wide erosion rates, denudation rates, and the degree of weathering in the Amazon basin

H. Wittmann[1], F. von Blanckenburg[1,2], N. Dannhaus[1], J. Bouchez[1,3], J. Gaillardet[3], J. L. Guyot[4], L. Maurice[5], H. Roig[6], N. Filizola[7], and M. Christl[8]

[1]Helmholtz Centre Potsdam, GFZ German Research Centre for Geosciences, Telegrafenberg, Potsdam, Germany, [2]Also at Institute of Geological Sciences, Freie Universität Berlin, Berlin, Germany, [3]Now at Institut de Physique du Globe de Paris- Université Paris Diderot, CNRS, Paris, France, [4]Instituto de Pesquisa para o Desenvolvimento (IRD), Lima, Peru, [5]GEToulouse, CNRS-IRD-Université de Toulouse, Toulouse, France, [6]Institute of Geosciences, University of Brasilia, Brasilia, Brazil, [7]Federal University of Amazonas, Manaus, Brazil, [8]Laboratory of Ion Beam Physics, ETH Zurich, Zurich, Switzerland

Abstract We present an extensive investigation of a new erosion and weathering proxy derived from the $^{10}Be(meteoric)/^{9}Be(stable)$ ratio in the Amazon River basin. This new proxy combines a radioactive atmospheric flux tracer, meteoric cosmogenic ^{10}Be, with ^{9}Be, a trace metal released by weathering. Results show that meteoric ^{10}Be concentrations ($[^{10}Be]$) and $^{10}Be/^{9}Be$ ratios increase by >30% from the Andes to the lowlands. We can calculate floodplain transfer times of 2–30 kyr from this increase. Intriguingly however, the riverine exported flux of meteoric ^{10}Be shows a deficit with respect to the atmospheric depositional ^{10}Be flux. Most likely, the actual area from which the ^{10}Be flux is being delivered into the mainstream is smaller than the basin-wide one. Despite this imbalance, denudation rates calculated from $^{10}Be/^{9}Be$ ratios from bed load, suspended sediment, and water samples from Amazon Rivers agree within a factor of 2 with published in situ ^{10}Be denudation rates. Erosion rates calculated from meteoric $[^{10}Be]$, measured from depth-integrated suspended sediment samples, agree with denudation rates, suggesting that grain size-induced variations in $[^{10}Be]$ are minimized when using such sampling material instead of bed load. In addition, the agreement between erosion and denudation rates implies minor chemical weathering intensity in most Amazon tributaries. Indeed, the Be-specific weathering intensity, calculated from mobilized ^{9}Be comprising reactive and dissolved fractions that are released during weathering, is constant at approximately 40% of the total denudation from the Andes across the lowlands to the Amazon mouth. Therefore, weathering in the Amazon floodplain is not detected.

1. Introduction

In the last few decades, significant methodological advances have been made that now allow accurate quantification of erosion and weathering rates over a range of temporal and spatial scales. This progress was essential to quantify physical and chemical weathering fluxes to address problems related to soil formation, sediment production, sediment source-to-sink relationships, and continental CO_2 consumption via weathering. To maintain this progress, development of new means to quantitatively determine terrigenous fluxes at the Earth's surface is required. The isotope ratio of the cosmogenic meteoric nuclide ^{10}Be to its stable counterpart ^{9}Be is such a new method. The $^{10}Be(meteoric)/^{9}Be(stable)$ ratio allows one to simultaneously determine erosion rates, denudation rates, and the degree of weathering [*von Blanckenburg et al.*, 2012]. We test this approach in the large Amazon basin, in which independent estimates of denudation and erosion rates are available.

Meteoric ^{10}Be reaches the Earth surface by dry and wet deposition and readily binds to fine-grained particles. Its concentration in non-eroding Earth surface deposits depends on their exposure time to fallout of this nuclide, and its concentration in mobile detrital sediment depends on erosion rate. *Brown* [1987] was the first one to recognize this and suggested to use meteoric ^{10}Be in sediment as a measure of soil erosion rate when compared to depositional meteoric fluxes (measured in rainwater). Based on this work, *Brown et al.* [1988] and *You et al.* [1988] extended the spatial scale of analysis from local soil profiles to large watersheds.

However, meteoric ^{10}Be has variable retentivity in river sediment such that it can be significantly partitioned into a dissolved phase at low pH, and its concentration is highly grain size dependent [*Willenbring and von Blanckenburg*, 2010]. Normalizing to a stable reference isotope, such as ^{9}Be, can circumvent these issues such that the resulting isotope ratio is not sensitive to differences in, for example, grain size [*von Blanckenburg et al*., 2012; *Wittmann et al*., 2012].

A conceptual framework for the meteoric system was recently presented by *von Blanckenburg et al*. [2012] in the form of a set of steady state mass balance equations. The basis for this framework is that after ^{10}Be reaches the Earth surface, it mixes in soil solutions with ^{9}Be released by mineral weathering and is partly incorporated into the "reactive" phase (adsorbed or coprecipitated into secondary solids). The ^{10}Be/^{9}Be ratio of the dissolved load of soil or river water and of the reactive phase of soils and sediment is therefore dependent on the flux of ^{9}Be released from minerals. Through sequential chemical extraction, these reactive (reac) phases, comprising adsorbed Be and Be coprecipitated into amorphous and crystalline phases such as Mn-Fe-(hydr-)-oxides, can be accessed and a ratio $(^{10}Be/^{9}Be)_{reac}$ can be measured. The chemical extraction technique developed by *Tessier et al*. [1979], *Bourlès et al*. [1989], and *Brown et al*. [1992] and modified by *Wittmann et al*. [2012] for river sediment is suited to separate the different geochemical pools of Be. *Wittmann et al*. [2012] showed that $(^{10}Be/^{9}Be)_{reac}$ ratios obtained by this extraction technique are independent of measured particle size. After leaching of the reactive Be components, the remaining silicate residual constitutes a mineral-bound (min) ^{9}Be fraction, which in combination with the ^{9}Be concentration of the parent rock ($[^{9}Be]_{parent}$) can be used to assess the degree of mobilization of ^{9}Be from primary minerals during chemical weathering [*von Blanckenburg et al*., 2012]. The average $[^{9}Be]_{parent}$ is close to 2.5×10^{-6} g/g for most felsic crustal rocks [*von Blanckenburg et al*., 2012]. Thus, it is likely that at large spatial scales such as the Amazon basin (~6×10^{6} km^2), the bedrock ^{9}Be concentration is close to this mean. From these ^{9}Be quantities the "mobilized" ^{9}Be flux fraction, its knowledge being a prerequisite to the determination of denudation rates, can be calculated. Lastly, what is needed for the application of the framework is knowledge of the flux of meteoric ^{10}Be that is delivered to the Earth's surface by dry and wet deposition. In the large Amazon basin, regional inaccuracies in meteoric deposition models [*Ouimet et al*., 2015] are most likely averaged out. We thus derive large-scale meteoric deposition rates from a combination of a model for the simulation of cosmic ray particle interactions with the Earth's atmosphere [*Masarik and Beer*, 1999] with the "fifth generation European Centre (ECHAM5)" general atmospheric circulation model (GCM) that is coupled to the aerosol model HAM [*Heikkilä et al*., 2013a, 2013b]. Therefore, the combined system of $(^{10}Be/^{9}Be)_{reac}$, $[^{9}Be]_{parent}$, and $[^{9}Be]_{min}$ provides rates of total denudation, erosion, and degree of weathering for entire river basins when measured in river water and sediment. The dissolved component of the ^{10}Be/^{9}Be ratio can also be used for denudation rate estimates provided the dissolved Be equilibrates isotopically with reactive Be (and ignoring a negligible mass-dependent isotope fractionation [*von Blanckenburg et al*., 2012]). We present a short summary of the mathematical framework for this method in section 1.1.

Here we test this new and promising proxy to quantify Earth surface processes in the large Amazon basin for all main tributaries (Table 1a). There recent work has provided kiloyear (kyr) time scale denudation rates and sediment fluxes from cosmogenic ^{10}Be produced in situ in quartz minerals from detrital river sediment [*Wittmann et al*., 2011a]. Modern, gauging-derived sediment fluxes [*Dunne et al*., 1998; *Guyot et al*., 2005, 1996; *Laraque et al*., 2005; *Martinez et al*., 2009; *Meade et al*., 1985; *Wittmann et al*., 2011a], discharge [*Coe et al*., 2002; *Filizola et al*., 2009; *Guyot*, 1993; *Moreira-Turcq et al*., 2003], and water chemistry and pH values [*Gaillardet et al*., 1997; *Moquet et al*., 2011] are also available. In addition, the first systematic study on the geochemistry of both ^{9}Be and ^{10}Be was carried out in the Amazon basin by *Brown et al*. [1992], who thoroughly investigated Be partitioning within the dissolved, leachable, and particulate pools. We perform this test in the Amazon basin with the aim (a) to evaluate the degree of ^{9}Be mobilization, (b) to explore whether the depositional flux of meteoric ^{10}Be is balanced with the sedimentary and dissolved flux out of the basin, such that the steady state of sediment transport can be evaluated, and (c) to evaluate whether the ^{10}Be/^{9}Be ratio has equilibrated between the dissolved and the sedimentary reactive phase. The final aims are (d) to derive degrees of weathering as a function of geomorphic setting and (e) to compare derived erosion and denudation rates with those from in situ cosmogenic ^{10}Be.

1.1. Conceptual Framework

Following the terminology of *von Blanckenburg et al*. [2012], the concentration of $[^{9}Be]_{parent}$ is partitioned during weathering between the reactive, dissolved, and residual mineral-bound Be, called $^{9}Be_{reac}$, $^{9}Be_{diss}$,

Table 1a. Sample and Basin Characteristics

Sample (ID as in *Wittmann et al.* [2009, 2011a])	Type	Basin	River	Setting	Latitude/ Longitude(° UTM)	Distance From Source Area[a](km)
Be 1 (average[b])	Bed load	Upper Madeira	Beni trunk	Bolivian Andes	−14.5273/−67.4969	0
Be-DSS	Suspended sediment	Suspended sediment depth profile (1.5 m to 4.5 m depth); location and basin characteristics similar to Be 1				
Be 1-W	River water	Location and basin characteristics similar to Be 1				
Be 2–1, 2-2[c]	Bed load	Upper Madeira	Beni trunk	Bolivian Andes	−14.2844/−67.4737	30
Be 3	Bed load	Upper Madeira	Beni trunk	Bolivian Andes	−13.5713/−67.3533	110
Be 4	Bed load	Upper Madeira	Beni trunk	Bolivian Andes	−13.1191/−67.1846	170
Be 8	Bed load	Upper Madeira	Beni trunk	Bolivian Andes	−12.0777/−66.8819	290
Be 10	Bed load	Upper Madeira	Beni trunk	Bolivian Andes	−11.5585/−66.6766	350
Be 12	Bed load	Upper Madeira	Beni trunk	Bolivian Andes	−11.2125/−66.2488	400
Md 15	Bed load	Upper Madeira	Madre de Dios	Bolivian Andes	−11.1123/−66.4159	415
Md-DSS	Suspended sediment	Suspended sediment depth profile (surface to 7 m depth); location and basin characteristics similar to Md 15				
Md 15-W	River water	Location and basin characteristics similar to Md 15				
OR 16	Bed load	Upper Madeira	Orthón	Bolivian Andes	−10.8200/−66.1100	450
Be 17	Bed load	Upper Madeira	Beni trunk	Bolivian Andes	−10.5500/−65.6000	510
Mar 18	Bed load	Marmoré/Madeira	Mamoré	Boliv. Andes/Braz. Shield	−10.8078/−65.3458	560
Mad 19	Bed load	Upper Madeira	Madeira	Boliv. Andes/Braz. Shield	−10.2292/−65.2811	570
Mad 20	Bed load	Upper Madeira	Madeira	Boliv. Andes/Braz. Shield	−8.7703/−63.9092	800
GR 19[b]	Bed load	Upper Madeira	Grande	Bolivian Andes	−18.9091/−63.4095	0
Pe 101	Bed load	Solimões	Solimões	Peruv.-Ecuad. Andes	−3.5988/−73.1373	830
Pe 107	Bed load	Solimões	Ucayali	Peruv.-Ecuad. Andes	−4.4794/−73.4263	700
Man 2.4[d]	Bed load	Amazon	Amazon at Manacapuru	Lowlands	−3.3202/−60.5541	2630
Ir 1.75[d]	Bed load	Amazon	Amazon at Iracema	Lowlands	−3.3288/−58.8287	2850
Ir-W	River water	Location and basin characteristics similar to sample Ir 1.75				
Par 0.9-2.2[d]	Bed load	Amazon	Amazon at Parintins	Lowlands	−3.4107/−58.7793	3090
Par-W	River water	Location and basin characteristics similar to Par 0.9				
Obi (average[b])	Bed load	Amazon	Amazon at Óbidos	Lowlands	−1.9359/−55.4989	3150
Obi-DSS	Suspended sediment	Suspended sediment depth profile (surface to 55 m depth)			−1.9348/−55.5052	
Obi-W	River water	Location and basin characteristics similar to Obi				
Mad 0.3-1.8[d]	Bed load	Lower Madeira	Madeira	Lowlands	−3.4055/−58.7913	1800
Mad-DSS	Suspended sediment	Suspended sediment depth profile (surface to 12 m depth); location and basin characteristics similar to Mad 0.3–1.8				
Mad-W1,2[e]	River water	Location and basin characteristics similar to Mad 0.3–1.8				
Cb 2 (average[b])	Bed load	Upper Madeira	Guaporé	Brazilian Shield	−13.4829/−61.0446	0
Cb 3	Bed load	Upper Madeira	Aripuana	Brazilian Shield	−10.1696/−59.4661	0
Cb 5	Bed load	Upper Tapajós	Apiacás	Brazilian Shield	−9.9357/−56.9372	0
Cb 6	Bed load	Upper Tapajós	Teles Pires	Brazilian Shield	−9.6391/−56.0191	0
Br 2	Bed load	Branco	Branco	Guyana Shield	1.8167/−61.0422	300
Br 3	Bed load	Branco	Branco	Guyana Shield	1.4099/−61.2786	360
Br 4	Bed load	Branco	Branco	Guyana Shield	1.3015/−61.2993	400
Br 7 (average[b])	Bed load	Branco	Branco	Guyana Shield	−0.3425/−61.8022	550
Ne 0.6[d]	Bed load	Negro	Negro	Guyana Shield	−3.0755/−60.2261	1000
Ne-W	River water	Location and basin characteristics similar to Ne 0.6				

[a]Measured along the Beni or the Solimões mainstem for all central Amazon samples.
[b]These data are taken from *Wittmann et al.* [2012] and denote averages when more than one sample or several grain sizes were measured.
[c]Be 2–2 denotes the replicate sample of Be 2–1.
[d]Number denotes distance from left bank (in km) where sample was dredged from river bottom, e.g., "Par 0.9" was sampled 900 m from left bank in river channel.
[e]Mad-W1 and Mad-W2 are analytical replicates from the same sample but processed by two different operators in different labs and measured at different AMS.

and $^{9}Be_{min}$, respectively. In combination with $[^{10}Be]_{reac}$ or $[^{10}Be]_{diss}$, we can derive the total denudation rate D, which is the sum of erosion (E, the rate at which solid material is removed from Earth's surface) plus weathering (W, being the dissolved component).

1.1.1. Steady State of ^{10}Be Fluxes

A requirement for using the framework presented by *von Blanckenburg et al.* [2012] and for calculating erosion rates using meteoric ^{10}Be in general is that the inputs of ^{10}Be into a drainage basin balance the outputs.

The basin-wide atmospheric input of ^{10}Be, $J^{^{10}Be}_{atm}$, at/yr, reaching the basin's surface area, is

$$J^{^{10}Be}_{atm} = \sum_{i=1}^{n} A_{riv,i} \times F^{^{10}Be}_{met,i} \quad (1)$$

where $A_{riv,i}$, m^2, is the surface area of a given subbasin i and $F^{^{10}Be}_{met,i}$, at/m^2/yr, is the meteoric flux of ^{10}Be.

The total meteoric flux of ^{10}Be exported by the river system, $J^{^{10}Be}_{riv}$, at/yr, is the sum of the riverine solid reactive (adsorbed and secondary solids) and dissolved fractions transported by the river, called $J^{^{10}Be}_{riv\_reac}$ and $J^{^{10}Be}_{riv\_diss}$, respectively (both in at/yr),

$$J^{^{10}Be}_{riv} = \left(J^{^{10}Be}_{riv\_reac} + J^{^{10}Be}_{riv\_diss}\right) \times \left(1 - \exp^{(-\lambda t)}\right) \quad (2)$$

where the right-hand term describes the basin-averaged radioactive decay of ^{10}Be during sediment transfer and storage with the decay constant λ (5×10^{-7} 1/yr, *Chmeleff et al.* [2010] and *Korschinek et al.* [2010], corresponding to a half-life of 1.39 Myr) and t the average sediment storage time.

By summing up the individual subbasins i, $J^{^{10}Be}_{riv}$ is

$$J^{^{10}Be}_{riv} = \sum_{i=1}^{n} \left[\left(A_{riv,i} \times E_i \times \left[^{10}Be\right]_{reac,i} + Q_i \times \left[^{10}Be\right]_{diss,i}\right) \times \left(1 - \exp^{(-\lambda t(i))}\right)\right] \quad (3)$$

where the subbasins i, having an area $A_{riv,i}$, are characterized by their individual reactive and dissolved concentrations $[^{10}Be]_{reac,i}$ in at/kg$_{solid}$ and $[^{10}Be]_{diss,i}$ in at/L$_{water}$, respectively, E_i is the erosion rate in kg/m^2/yr, derived from in situ ^{10}Be or modern sediment loads from gauging (Table 1b), Q_i the basins discharge in L/yr, and $t(i)$ the sediment storage time in each subbasin. The decay term of equations (2) and (3) becomes negligible for settings where the time scale of storage of sediment is short (e.g., such as the Andes) compared to the half-life of ^{10}Be. The balance of ^{10}Be fluxes is attained if

$$J^{^{10}Be}_{riv} = J^{^{10}Be}_{atm} \quad (4)$$

Consequently, the ^{10}Be inventory of the basin is at steady state if $J^{^{10}Be}_{riv}/J^{^{10}Be}_{atm} = 1$.

1.1.2. A Chemical Weathering Intensity Proxy Based on Stable ^{9}Be

A parent ^{9}Be is contained in bedrock (g/kg$_{rock}$) and is then during weathering partitioned into reactive and dissolved ^{9}Be fractions ($[^{9}Be]_{reac}$, g/kg$_{solid}$, and $[^{9}Be]_{diss}$, g/L$_{water}$) that are carried along with sediment and with discharge, respectively. Unlike ^{10}Be, however, a fraction of lattice-bound ^{9}Be will remain in primary minerals of soils and sediment ($[^{9}Be]_{min}$, g/kg$_{solid}$) during incongruent weathering. Only the mobilized flux fraction of reactive and dissolved ^{9}Be, called $\left(f^{^{9}Be}_{reac} + f^{^{9}Be}_{diss}\right)$, is available for mixing with ^{10}Be in the weathering zone [*von Blanckenburg et al.*, 2012]. There are two independent means to determine $\left(f^{^{9}Be}_{reac} + f^{^{9}Be}_{diss}\right)$. First, $\left(f^{^{9}Be}_{reac} + f^{^{9}Be}_{diss}\right)$ may be calculated from river fluxes. Following the formalism defined in *von Blanckenburg et al.* [2015], the total riverine ^{9}Be flux $J^{^{9}Be}_{riv}$, g/yr, is the sum of the fluxes of riverine solid reactive $J^{^{9}Be}_{riv}$, solid residual $J^{^{9}Be}_{riv}$, and dissolved transport $J^{^{9}Be}_{riv}$ (all in g/yr):

$$\begin{aligned} J^{^{9}Be}_{riv} &= J^{^{9}Be}_{riv\_reac} + J^{^{9}Be}_{riv\_min} + J^{^{9}Be}_{riv\_diss} \\ &= A_{riv} \times E \times \left([^{9}Be]_{reac} + [^{9}Be]_{min}\right) + Q \times [^{9}Be]_{diss} \end{aligned} \quad (5)$$

For large rivers, individual subbasins i are summed up:

$$J^{^{9}Be}_{riv} = \sum_{i=1}^{n} \left(A_{riv,i} \times E_i \times \left(\left[^{9}Be\right]_{reac,i} + \left[^{9}Be\right]_{min,i}\right) + Q_i \times \left[^{9}Be\right]_{diss,i}\right) \quad (6)$$

Nondimensional ^{9}Be fluxes can be derived for each individual flux in equation (5) by dividing by the total ^{9}Be flux $J^{^{9}Be}_{riv}$:

$$f^{^{9}Be}_{reac} = \frac{J^{^{9}Be}_{riv\_reac}}{J^{^{9}Be}_{riv}} \quad (7a)$$

$$f^{^{9}Be}_{diss} = \frac{J^{^{9}Be}_{riv\_diss}}{J^{^{9}Be}_{riv}} \quad (7b)$$

Table 1b. Sample and Basin Characteristics Continued

Sample (ID as in *Wittmann et al.* [2009, 2011a])	Total Drainage Area ($\times 10^4$ km^2)	Area of High-Relief Source[a] ($\times 10^4$ km^2)	Water Discharge[b] (m^3/s)	In Situ-Derived Basin-Wide Denudation Rate[c](mm/yr)	In Situ-Derived Floodplain-Corrected Denudation Rate[d] (mm/yr)	Modern Suspended Sediment Load[e] ($\times 10^6$ t/yr)	Riverine pH Value[f]	Basin-Wide Precipitation[g] (mm/yr)
Be 1 (average[h])	6.75	6.75	2,050	0.375 ± 0.063	0.375 ± 0.063	212	6.1–8.4	
Be-DSS								
Be 1-W								
Be 2-1, 2-2[i]	7.30	6.75	2,050	0.68 ± 0.15	0.69 ± 0.15	212		
Be 3	8.04	6.75	2,050	0.395 ± 0.052	0.454 ± 0.057	212		
Be 4	9.29	6.75	2,050	0.156 ± 0.020	0.212 ± 0.025	212		
Be 8	11.0	6.75	2,050	0.250 ± 0.036	0.404 ± 0.051	212		1,725
Be 10	11.3	6.75	2,050	0.207 ± 0.022	0.345 ± 0.032	212		
Be 12	12.4	6.75	3,772	0.195 ± 0.049	0.353 ± 0.084	122		
Md 15	14.0	6.94	5,600	0.28 ± 0.13	0.28 ± 0.13	71	5.2–7.3	
Md-DSS								
Md 15-W								
OR 16	3.21	3.21	475	0.0332 ± 0.0039	0.0332 ± 0.0039	1.8	7.1–7.7	
Be 17	30.4	6.75	9,780	0.168 ± 0.031	0.389 ± 0.069	191	6.3–7.4	
Mar 18	59.9	12.3	8,400	0.084 ± 0.025	0.189 ± 0.058	66	5.8–8.6	
Mad 19	88.2	26.0	18,520	0.116 ± 0.017	0.263 ± 0.038	148[j]		
Mad 20	95.4	26.0	19,360	0.129 ± 0.014	0.300 ± 0.035	230		
GR 19[h]	5.98	5.98	360	0.625 ± 0.090	0.630 ± 0.090	138		
Pe 101	73.3	73.3	30,150	0.147 ± 0.015	0.204 ± 0.021	413	6.7–8.0	
Pe 107	36.0	36.0	12,090	0.260 ± 0.029	0.337 ± 0.036	205	6.8–7.4	
Man 2.4[k]	227	50.0	98,970	0.098 ± 0.010	0.241 ± 0.025	569	6.9–7.6	2,900
Ir 1.75[k]	315	62.8		0.0863 ± 0.0093	0.243 ± 0.026	785	6.8	
Ir-W								
Par 0.9-2.2[k]	474	62.8	88,695	0.0784 ± 0.0082	0.211 ± 0.022	785	6.8	
Par-W								
Obi (average[h])	509	62.8	169,480	0.0680 ± 0.0059	0.197 ± 0.020	939	6.9	
Obi-DSS								
Obi-W								
Mad 0.3-1.8[k]	144	28.2	31,200	0.089 ± 0.010	0.206 ± 0.023	433	6.8	1,940
Mad-DSS								
Mad-W1,2[l]								
Cb 2 (average[h])	11.0	11.0	915	0.0274 ± 0.0033	0.0274 ± 0.0033		5.3–7.3	
Cb 3	2.01	2.01	3,400	0.0110 ± 0.0013	0.0110 ± 0.0013			
Cb 5	1.22	1.22		0.01510 ± 0.00095	0.0151 ± 0.0009			
Cb 6	9.37	9.37	1,178	0.0251 ± 0.0024	0.0251 ± 0.0024			
Br 2	14.7	14.7	2,865	0.00992 ± 0.00073	0.01200 ± 0.00082	3.3[m]	6.4–7.0	
Br 3	14.9	14.9	2,865	0.00992 ± 0.00073	0.01200 ± 0.00082	3.3[m]	6.4–7.0	
Br 4	15.1	15.1	2,865	0.01112 ± 0.00079	0.01200 ± 0.00082	3.3[m]	6.4–7.0	
Br 7 (average[h])	21.1	21.1	3,350	0.0108 ± 0.0010	0.01200 ± 0.00082	3.3[m]	6.4–7.0	
Ne 0.6	83.2	83.2	28,400	0.0438 ± 0.0037	0.0438 ± 0.0037	8.5	4.2–5.2	2,566
Ne-W								

[a] Floodplain-corrected drainage area (i.e., excluding low-relief areas; see *Wittmann et al.* [2009, 2011a]).
[b] Water discharge is from *Guyot* [1993], *Coe et al.* [2002], *Moreira-Turcq et al.* [2003], *Filizola et al.* [2009], and *Moquet et al.* [2011].
[c] Taken from *Wittmann et al.* [2009, 2011a]. Rates are basin-wide rates (no "floodplain correction" applied).
[d] Taken from *Wittmann et al.* [2009, 2011a]. Floodplain correction removes lowland contribution to ^{10}Be production and thus derived rates are "sediment production rates"; i.e., they measure the source-area derived erosion.
[e] For original data sources, we refer to the tables of *Wittmann et al.* [2009, 2011a].
[f] Riverine pH values from *Gaillardet et al.* [1997], *Maurice et al.* [1999], *Moquet et al.* [2011], *Allard et al.* [2002], *Moreira-Turcq et al.* [2003], and *Silva et al.* [2006].
[g] Basin-wide precipitation is from *Espinoza Villar et al.* [2009] and *Moreira-Turcq et al.* [2003].
[h] These data are taken from *Wittmann et al.* [2012] and denote averages when more than one sample or several grain sizes were measured.
[i] Be 2-2 denotes the replicate sample of Be 2-1.
[j] Average from Mad 18 and Mad 20.
[k] Number denotes distance from left bank (in km) where sample was dredged from river bottom; e.g., "Par 0.9" was sampled 900 m from left bank in river channel.
[l] Mad-W1 and Mad-W2 are analytical replicates from the same sample but processed by two different operators in different labs and measured at different AMS.
[m] Value was measured by *Moreira-Turcq et al.* [2003] at the outlet of the Branco River.

The fraction of ^{9}Be mobilized by the rivers' sedimentary and water fluxes, $(f_{reac} + f_{diss})_{fluxes}$, is

$$(f_{reac} + f_{diss})_{fluxes} = \frac{J^{^9Be}_{riv\_reac} + J^{^9Be}_{riv\_diss}}{J^{^9Be}_{riv}} = \frac{A_{riv} \times E \times [^9Be]_{reac} + Q \times [^9Be]_{diss}}{A_{riv} \times E \times ([^9Be]_{reac} + [^9Be]_{min}) + Q \times [^9Be]_{diss}} \quad (8)$$

In some cases, information on solid and dissolved ^{9}Be fluxes is not available. Then, a second means to derive $\left(f^{^9Be}_{reac} + f^{^9Be}_{diss}\right)$ can then be used that is based on measured $[^9Be]_{reac}$ and $[^9Be]_{min}$ in sediment (derived by combining equations (9) and (12) in *von Blanckenburg et al.* [2012]):

$$(f_{reac} + f_{diss})_{min/reac} = \frac{1}{\left(\frac{[^9Be]_{min}}{[^9Be]_{reac}} + 1\right)} \quad (9)$$

This method works best if the degree of weathering of the sediment is sufficiently high, i.e., when $q/D \times f^{^9Be}_{min} \ll K_d$ (as is equation (12) in *von Blanckenburg et al.* [2012]), where q (L/km^2/yr) is the runoff (area-normalized water discharge), and K_d (L/kg) is the partition coefficient accounting for the distribution of Be between the reactive and the dissolved phases that is highly pH dependent [*Aldahan et al.*, 1999; *Brown et al.*, 1992]. K_d can be calculated from the ratio of $[Be]_{reac}$ to $[Be]_{diss}$ or is available from the literature [e.g., *You et al.*, 1989]. We must bear in mind, however, that a bias might be contained in equation (9) as $[^9Be]_{reac}$ is potentially enriched over $[^9Be]_{min}$ in finer grain sizes by particle sorting [*von Blanckenburg et al.*, 2012].

1.1.3. Erosion Rates Based on Meteoric ^{10}Be

The following steady state mass balance equation allows the derivation of full erosion rates $E_{[^{10}Be]full}$ (corrected for retentivity, see below) and simplified (uncorrected for retentivity) $E_{[^{10}Be]_{reac}}{}'$, in kg/m^2/yr, from $[^{10}Be]_{reac}$ and $F^{^{10}Be}_{met}$ [*Brown et al.*, 1988; *von Blanckenburg et al.*, 2012; *Willenbring and von Blanckenburg*, 2010]:

$$E_{[^{10}Be]full} = \frac{F^{^{10}Be}_{met}}{[^{10}Be]_{reac}} - \frac{q}{K_d} \quad (10)$$

$$E_{[^{10}Be]}{}' = \frac{F^{^{10}Be}_{met}}{[^{10}Be]_{reac}} \quad (11)$$

The second, right-hand term of equation (10) introduced by *von Blanckenburg et al.* [2012] represents the correction for ^{10}Be partitioning into the dissolved phase. Thus, this equation provides accurate erosion rates only if q and K_d are known over the residence time of Be in the weathering zone. The simplified equation (11) ($E_{[^{10}Be]}{}'$) (ignoring the q/K_d term in equation (10)) can be used in settings where retentivity of ^{10}Be is high in the solid phase [*Brown et al.*, 1988; *Willenbring and von Blanckenburg*, 2010]. In these settings ^{10}Be is almost entirely sorbed onto particles or precipitated and is not significantly exported as a solute. Such conditions are encountered in settings with low water discharge or high erosion rates, or when pH >6 [*von Blanckenburg et al.*, 2012]. Importantly, $[^{10}Be]_{reac}$ also depends on grain size, as ^{10}Be is preferentially sorbed onto or is precipitated into fine particles [*Shen et al.*, 2004; *Willenbring and von Blanckenburg*, 2010; *Wittmann et al.*, 2012]. Thus, derived erosion rates mostly depend on grain size, such that the $[^{10}Be]_{reac}$ measured in a given river sediment sample are not necessarily recording the "right," or representative, erosion rate.

1.1.4. Denudation Rates Based on $(^{10}Be/^{9}Be)_{reac}$ and $(^{10}Be/^{9}Be)_{diss}$ Ratios

Combining the two mass balance approaches for ^{10}Be and stable ^{9}Be results in $(^{10}Be/^{9}Be)_{reac}$ and $(^{10}Be/^{9}Be)_{diss}$ ratios. These ratios are a function of denudation rate D, $\left(f^{^9Be}_{reac} + f^{^9Be}_{diss}\right)$, and $[^9Be]_{parent}$. If fractional fluxes (equations (8) or (9)) are known, a flux-based denudation rate D_MET$_{fluxes}$, kg/m^2/yr, can be calculated based on equation (9) in *von Blanckenburg et al.* [2012]:

$$D\_MET_{fluxes} = \frac{F^{^{10}Be}_{met}}{\left(\frac{^{10}Be}{^{9}Be}\right)_{reac/diss} \times [^9Be]_{parent} \times \left(f^{^9Be}_{reac} + f^{^9Be}_{diss}\right)} \quad (12)$$

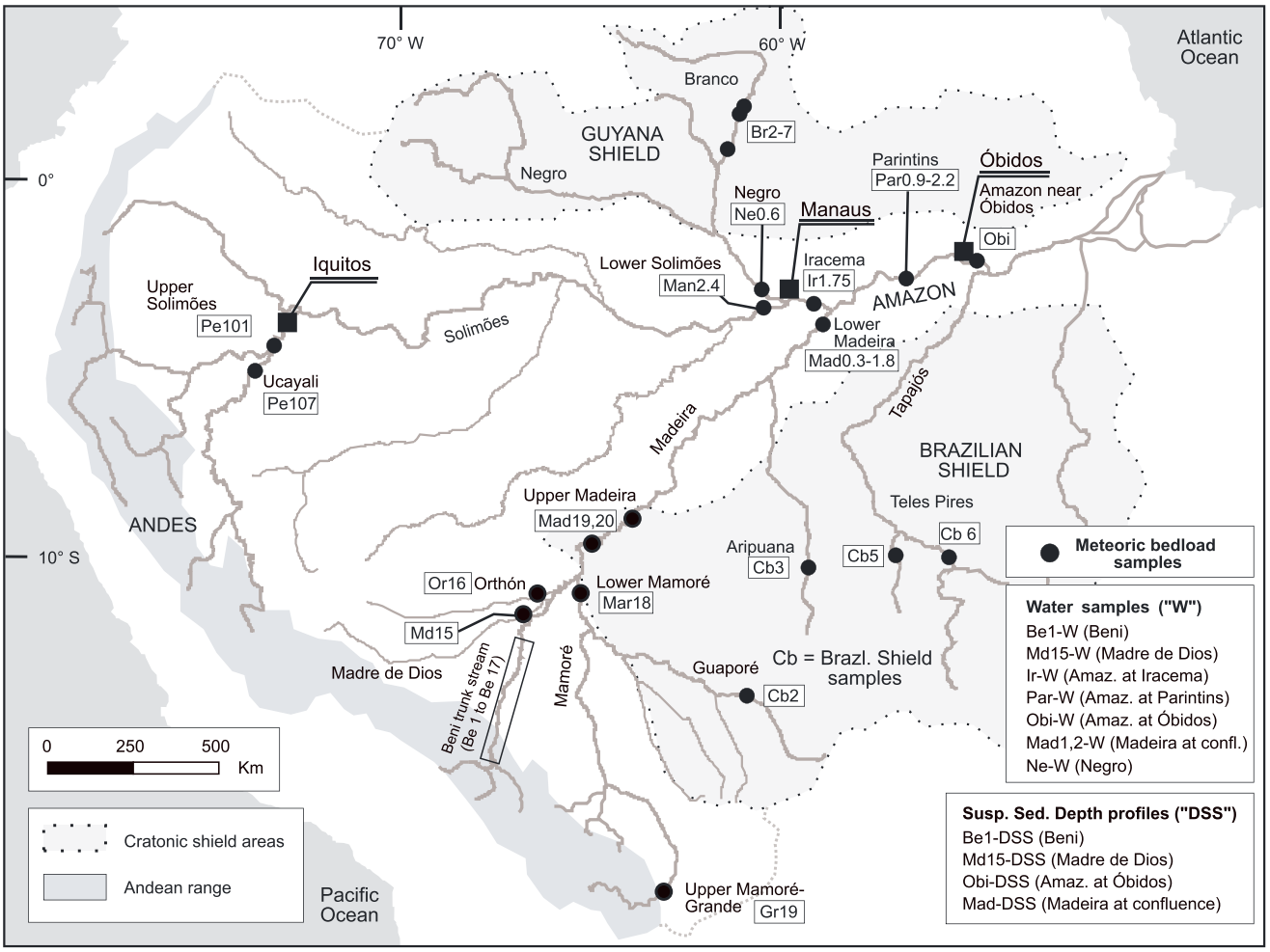

Figure 1. Study area and sampling locations. Bed load samples (using mainly the 30–40 μm grain size fraction) are marked by black circles. Suspended sediments were analyzed for four depth profiles (see text box "DSS"). ^{10}Be analyses in river water are available at seven locations (see text box "W").

Another approach to calculate denudation rates can be used if the ^{9}Be fluxes are not known. Solving equation (10) in *von Blanckenburg et al.* [2012] for denudation rate D results in retentivity-corrected D_MET$_{min/reac\text{-}full}$ that incorporate the ratio of $^{9}Be_{min}$ over $^{9}Be_{reac}$ instead of using $(f_{reac}+f_{diss})_{fluxes}$:

$$\mathrm{D\_MET}_{min/reac\text{-}full} = \frac{F_{met}^{^{10}Be}}{\left(\frac{^{10}Be}{^{9}Be}\right)_{reac/diss} \times [^{9}Be]_{parent}} \times \left(\frac{[^{9}Be]_{min}}{[^{9}Be]_{reac}} + 1\right) - \frac{q}{K_d} \times \frac{[^{9}Be]_{min}}{[^{9}Be]_{parent}} \quad (13)$$

If the following condition is met,

$$\frac{q}{D} \times f_{min}^{^{9}Be} \ll K_d \quad (14)$$

the negative, right-hand term in equation (13) can be ignored, and a simplified equation (15) can be used to calculate simplified denudation rates (D_MET$_{min/reac}$′):

$$\mathrm{D\_MET}_{min/reac}{}' = \frac{F_{met}^{^{10}Be}}{\left(\frac{^{10}Be}{^{9}Be}\right)_{reac/diss} \times [^{9}Be]_{parent}} \times \left(\frac{[^{9}Be]_{min}}{[^{9}Be]_{reac}} + 1\right) \quad (15)$$

Bias on this D_MET$_{min/reac}$′ is small in case of high retentivity for Be and low runoff q, and high degrees of weathering such that $f_{min}^{^{9}Be} \ll 1$ or $\left(f_{reac}^{^{9}Be} + f_{diss}^{^{9}Be}\right)$ is high (see appendix in *von Blanckenburg et al.* [2012] for a detailed assessment of this bias). Note that for a given K_d, these conditions are the same as those that hold for simplifying equation (10).

Table 2. Meteoric ^{10}Be, ^{9}Be, and ^{10}Be/^{9}Be Ratio Data for Bed Load Samples[a]

		Sample Weight for "Min" and "Leach" Fractions		Fraction Leach (Summed Am-Ox + X-Ox Extractions)				Fraction Min (Silicate Residue)	
Sample	Grain Size Fraction of Bed Load (μm)	Initial Solid Sample Weight (First ^{9}Be Batch) (g)	Initial Solid Sample Weight (Second ^{9}Be Batch)[b] (g)	$[^{10}Be]_{reac}$ ($\times 10^{4}$ at/g$_{solid}$)	$[^{9}Be]_{reac}$ (First Batch) ($\times 10^{-9}$ g/g$_{solid}$)	$[^{9}Be]_{reac}$ (Second Batch) ($\times 10^{-9}$ g/g$_{solid}$)	$(^{10}Be/^{9}Be)_{reac}$[c] ($\times 10^{-10}$)	$[^{10}Be]_{min}$ ($\times 10^{4}$ at/g$_{solid}$)	$[^{9}Be]_{min}$[d] ($\times 10^{-9}$ g/g$_{solid}$)
Be 1 (average)	all	NA	-	753 ± 43	448 ± 22	450 ± 16	2.43 ± 0.20	45 ± 15	999 ± 48
Be 2-1	30–40	0.5055	0.5885	619 ± 58	405 ± 20	-	2.29 ± 0.24	45 ± 16	953 ± 46
Be 2-2	30–40	-	-	541 ± 44	374 ± 19	399 ± 14	2.09 ± 0.21	-	-
Be 3	30–40	0.5001	-	573 ± 40	372 ± 19	-	2.31 ± 0.20	-	-
Be 4	30–40	0.4504	-	595 ± 44	430 ± 21	-	2.07 ± 0.18	26 ± 13	-
Be 8	30–40	0.5016	-	445 ± 26	314 ± 16	-	2.12 ± 0.16	46 ± 13	-
Be 10	30–40	0.5092	0.5170	510 ± 35	338 ± 17	357 ± 13	2.20 ± 0.20	27 ± 13	1,149 ± 56
Be 12	30–40	0.5034	-	547 ± 89	358 ± 18	-	2.29 ± 0.39	37 ± 13	-
Md 15	30–40	0.5020	0.5149	760 ± 41	383 ± 19	407 ± 14	2.88 ± 0.23	36 ± 13	1,052 ± 52
OR 16	30–40	0.4977	-	1,687 ± 75	257 ± 13	-	9.83 ± 0.66	232 ± 24	-
Be 17	30–40	0.5020	0.5080	591 ± 40	320 ± 16	330 ± 12	2.72 ± 0.25	56 ± 16	1,243 ± 60
Mar 18	30–40	0.5000	0.4762	858 ± 46	303 ± 15	321 ± 11	4.12 ± 0.33	91 ± 17	1,036 ± 51
Mad 19	30–40	0.5001	-	775 ± 45	386 ± 19	-	3.01 ± 0.23	65 ± 16	-
Mad 20	30–40	0.5019	0.5340	1,193 ± 53	289 ± 14	307 ± 11	5.99 ± 0.45	31 ± 12	1,024 ± 50
GR 19	30–40	1.2125	-	493 ± 34	523 ± 26	-	1.41 ± 0.12	42 ± 7	910 ± 45
Pe 101	30–40	0.5047	0.5121	636 ± 42	235 ± 12	259 ± 10	3.85 ± 0.35	59 ± 16	919 ± 45
Pe 107	30–40	0.5004	-	453 ± 36	197 ± 10	-	3.44 ± 0.32	91 ± 20	-
Man 2.4	30–40	0.5000	-	1,292 ± 69	242 ± 12	-	7.98 ± 0.59	252 ± 38	-
Ir 1.75	30–40	0.4963	-	2,530 ± 115	441 ± 22	-	8.60 ± 0.58	134 ± 24	-
Par 0.9	30–40	0.5051	0.2176	2,710 ± 158	403 ± 20	358 ± 14	10.67 ± 0.92	272 ± 28	941 ± 47
Par 1.2	30–62	0.5007	-	1,395 ± 64	266 ± 13	-	7.84 ± 0.53	135 ± 20	-
Par 1.6	30–40	0.4496	0.5032	1,044 ± 53	277 ± 14	253 ± 9	5.90 ± 0.48	129 ± 18	915 ± 45
Par 2.2	30–40	0.4994	-	2,746 ± 124	394 ± 20	-	10.42 ± 0.70	283 ± 31	-
Obi (average)	all	NA	-	1,479 ± 63	305 ± 15	246 ± 9	7.08 ± 0.51	141 ± 16	661 ± 33
Mad 0.3	30–40	-	0.5375	2,389 ± 84	642 ± 32	657 ± 23	5.51 ± 0.39	-	1,332 ± 65
Mad 0.5	30–62	0.5003	0.5539	1,057 ± 53	320 ± 16	333 ± 12	4.85 ± 0.38	76 ± 18	1,524 ± 72
Mad 1.8	30–40	-	-	7,038 ± 247	1,140 ± 57	-	9.24 ± 0.56	-	-
Cb 2 (average)	all	NA	-	10,880 ± 353	269 ± 13	368 ± 14	52.5 ± 3.8	247 ± 27	559 ± 28
Cb 3	30–40	-	0.5089	19,670 ± 590	838 ± 42	850 ± 35	34.9 ± 2.5	-	919 ± 45
Cb 5	30–62	-	0.5210	6,152 ± 185	220 ± 11	209 ± 8	42.9 ± 3.0	-	794 ± 39
Cb 6	30–62	-	0.5536	12,400 ± 361	403 ± 20	409 ± 15	44.4 ± 3.1	-	913 ± 45
Br 2	90–125	-	-	2,440 ± 122	156.7 ± 7.8	-	23.3 ± 1.6	-	-
Br 3	125–250	0.9880	-	963 ± 54	70.7 ± 3.5	-	20.4 ± 1.5	156 ± 13	129.6 ± 6.5
Br 4	125–250	-	-	1,499 ± 65	102.5 ± 5.1	-	21.9 ± 1.4	-	-
Br 7 (average)	all	NA	-	1,393 ± 64	74.8 ± 3.8	-	32.8 ± 2.7	952 ± 55	752 ± 37
Ne 0.6	125–250	1.1458	-	399 ± 24	57.3 ± 2.9	-	10.41 ± 0.83	106 ± 10	200 ± 10

[a]NA = Not applicable; all uncertainties denote 1σ analytical uncertainties. For stable ^{9}Be measurements using ICP-OES, a 5% uncertainty is given that represents long-term repeatability. For ^{10}Be measurements, a blank ratio of $2.51 \pm 1.2 \times 10^{-15}$ ($n = 11$) was substracted, and the error was propagated into ^{10}Be concentrations. All bed load ^{10}Be data were measured at ETH Zurich; if measured before April 2010 (using the S555 standard with a nominal value of 95.5×10^{-12}), concentrations were corrected for the new standard (S555N, nominal value of 87.1×10^{-12}) according to the new ^{10}Be half-life [see *Kubik and Christl*, 2010].
[b]A second sample batch with newly weighed samples was processed repeating all steps to check consistency of the extraction procedure.
[c]Ratios were calculated using a ^{9}Be concentration averaged from first and second batches where possible.
[d]Most values obtained during second batch.

These denudation and erosion rates are presented in units of kg/m^2/yr. To compare them to *D* derived from in situ ^{10}Be (D_insitu) that are commonly presented in units of m/yr, we use a bedrock density of 2600 kg/m^3 for conversion.

2. Study Area, Samples, and Previous Work Using In Situ ^{10}Be in the Amazon Basin

2.1. Study Area and Sampling

The Amazon basin has three distinct geomorphic parts (Figure 1): (1) the Andean range characterized by rapid erosion on steep slopes drained by rivers having high suspended sediment loads, low organic matter contents, and pH values of 6–7 [*Gaillardet et al.*, 1997] and (2) the slowly eroding, tectonically quiescent tropical Guyana and Brazilian Shields that feature subdued mountains covered with thick lateritic soils.

These regions are drained by rivers with high dissolved humic concentrations (causing low pH values near 4), and low suspended sediment yields [*Edmond et al*., 1995; *Sioli*, 1968]. (3) The central Amazon lowlands are characterized by seasonally inundated relatively flat floodplains. Mean water discharge, riverine pH values, and mean annual rainfall for sampled rivers and basins are given in Tables 1a and 1b.

From these different climatic and geomorphic zones, we characterized the water and sediment pools of Be (Figure 1). The chemical composition of river sediment differs with grain size [*Bouchez et al*., 2011a]. This is in particular the case for $[^{10}Be]_{reac}$ [*Wittmann et al*., 2012]. Therefore, it is necessary to sample a representative range of grain sizes transported by a given river, from coarse bed load to fine suspended sediment transported near the water surface. We sampled a total of 30 coarse-grained bed load samples distributed among river basins of all three geomorphic zones (Table 1a) that were mainly dredged from channel bottoms. Note that the coarse fraction ($>$125 μm) of the same bed load samples was used by *Wittmann et al*. [2009, 2011a] for in situ ^{10}Be analysis whereas here we mainly used the 30–40 μm grain size fraction (Table 2). Further, we sampled suspended sediment depth profiles (termed DSS hereafter) in two major Andean rivers (Beni, Madre de Dios) and two depth profiles in the lower Madeira and the main Amazon at Óbidos that provide a range of grain sizes from fine particles near the channel surface to coarser particles near the channel bottom (see Table 3 for sampling depths). Water samples were taken from the main rivers draining the Andes (Beni, Madre de Dios) and the lowlands (Amazon at various places, lower Madeira) as well as from the Negro near its confluence with the Amazon, a river that drains the Guyana Shield. Detailed sampling information is given in section S1 in the supporting information.

2.2. Summary of Previous Findings Using In Situ ^{10}Be and ^{26}Al/^{10}Be Ratios in the Amazon Basin

Using the sand-sized bed load fraction of the same samples used here, *Wittmann et al*. [2009, 2011a] measured in situ ^{10}Be and *Wittmann et al*. [2011b] measured ^{26}Al/^{10}Be ratios in the Amazon basin. This ratio is sensitive to sediment storage and burial from the relative decay of in situ-produced ^{26}Al to the slower decaying ^{10}Be. The main findings of these studies were that the distinct denudation rates of a given source area (Andes versus cratonic shields) are preserved in in situ ^{10}Be nuclide concentrations measured in different bed load grain size fractions in downstream lowland reaches.

Fine sand-sized sediment (mostly 125–250 μm) preserves low Andean in situ ^{10}Be nuclide concentrations that are uniform from the Andean source down to Óbidos in the lowlands. These low in situ nuclide concentrations are equivalent to high Andean denudation rates of approximately 0.35 mm/yr that contribute the major portions of sediment to the lowlands. Coarse-sized sand (500 to 800 μm) preserves higher in situ ^{10}Be concentrations eroded from the cratonic shields that today do not contribute much sediment to the lower reaches but may have done so in, for example, Pleistocene times [*Latrubesse*, 2015]. Low ^{26}Al/^{10}Be ratios measured indicate previous burial for several million years of mainly shield-derived coarser sediment. A burial end-member that is tapped during avulsions shows burial ages of $>$3 Myr stored at depths of 10–20 m that is now incorporated into lowland floodplains, whereas ^{26}Al/^{10}Be ratios in Andean-derived fine-grained sandy sediment are compatible with a range from minor ($<$0.5 Myr) burial durations to the complete absence of burial.

If the denudation rate of the entire Amazon basin including the lowlands is to be determined, a floodplain-uncorrected denudation rate, termed "D_insitu" is calculated. Such a rate is based on the assumption that the entire basin provides sediment, and hence, the in situ cosmogenic nuclide production rate is scaled, as a function of altitude and latitude, for the entire basin. If, however, the assumption is that the lowlands do not produce any additional sediment and merely serve as a transfer route of sediment-produced upstream, the in situ ^{10}Be cosmogenic nuclide production rate is scaled for the Andes, excluding the low-altitude floodplain portion. In that case a "floodplain-corrected" denudation rate, termed "D_insitu_{FP}" here, can be calculated. This approach is justified if the concentrations of in situ-produced nuclides do not change in the lowlands (due to, for example, long-term storage and burial), such that they reflect those set in the eroding uplands. In this case, a mean sediment production rate of an entire mountain belt can be determined from samples collected downstream. An advantage of this large-basin approach is that it averages out the large variability present in denudation rates from small source area basins by riverine mixing [*Wittmann et al*., 2009]. Due to the averaging time scale of the in situ method, these Andean sediment production rates are estimated at over approximately 1 to 5 kyr, depending on denudation rate [*von Blanckenburg*, 2005].

The kiloyear-scale sediment budget estimated from these in situ-derived denudation rates shows that the Andes contribute most of the sediment to the Amazon mouth. As the lowland area does not contribute

Journal of Geophysical Research: Earth Surface

10.1002/2015JF003581

Table 3. Meteoric ^{10}Be, ^{9}Be, and ^{10}Be/^{9}Be Ratio Data for Suspended Sediment Samples (Depth Profiles)[a]

				Am-Ox and X-Ox Extractions and Summed "Reac" Fraction									Fraction Min (Silicate Residue)	
Sample (Water Depth in m)	Original Sample Code[b]	Al/Si[c]	Initial Solid Weight(g)	$[^{10}Be]_{am\text{-}ox}$ ($\times 10^{4}$ at/g_{solid})	$[^{10}Be]_{x\text{-}ox}$ ($\times 10^{4}$ at/g_{solid})	$[^{10}Be]_{reac}$ ($\times 10^{4}$ at/g_{solid})	$[^{9}Be]_{am\text{-}ox}$ ($\times 10^{-9}$ g/g_{solid})	$[^{9}Be]_{x\text{-}ox}$ ($\times 10^{-9}$ g/g_{solid})	$[^{9}Be]_{reac}$ ($\times 10^{-9}$ g/g_{solid})	$(^{10}Be/^{9}Be)_{am\text{-}ox}$ ($\times 10^{-10}$)	$(^{10}Be/^{9}Be)_{x\text{-}ox}$ ($\times 10^{-10}$)	$(^{10}Be/^{9}Be)_{reac}$ ($\times 10^{-10}$)	$[^{10}Be]_{min}$ ($\times 10^{4}$ at/g_{solid})	$[^{9}Be]_{min}$ ($\times 10^{-9}$ g/g_{solid})
Beni Depth Profile (Sampled in 2007; Mean Depth-Integrated Grain Size [D90] = 133 μm)														
Be-DSS-1.5 m	Am-07-03	0.321	0.0693	1055 ± 68	680 ± 58	1735 ± 130	640 ± 32	630 ± 31	1270 ± 63	2.48 ± 0.20	1.61 ± 0.16	2.05 ± 0.18	-	1975 ± 99
Be-DSS-4.5 m	Am-07-01	0.167	0.0994	535 ± 43	515 ± 41	1050 ± 85	350 ± 17	470 ± 23	820 ± 41	2.31 ± 0.22	1.64 ± 0.15	1.93 ± 0.18	-	1280 ± 64
Depth-integrated value[d]:		0.34		996	640	1810	673	646	1325	2.21	1.48	2.05		2060
Madre de Dios Depth Profile (sampled 2007; Mean Depth-Integrated Grain Size [D90] = 79 μm)														
Md-DSS-0 m	Am-07-14	0.343	0.1110	1695 ± 82	795 ± 47	2490 ± 130	740 ± 37	710 ± 35	1450 ± 72	3.45 ± 0.24	1.68 ± 0.13	2.58 ± 0.19	-	1480 ± 74
Md-DSS-7 m	Am-07-11	0.101	0.1678	1110 ± 53	430 ± 31	1540 ± 85	520 ± 26	520 ± 26	1040 ± 52	3.17 ± 0.22	1.24 ± 0.11	2.20 ± 0.16	-	1380 ± 69
Depth-integrated value[d]:		0.34		1580	640	2480	733	706	1440	3.23	1.36	2.57		1480
Óbidos Depth Profile (Sampled in 2006; Mean Depth-Integrated Grain Size [D90] = 82 μm)														
Obi-DSS-0 m	Am-06-59	0.398	0.0509	3440 ± 170	880 ± 77	4320 ± 250	820 ± 49	430 ± 22	1250 ± 71	6.27 ± 0.49	3.05 ± 0.31	5.16 ± 0.42	480 ± 55	1150 ± 77
Obi-DSS-10 m	Am-06-58	0.331	0.1101	2750 ± 140	805 ± 49	3555 ± 190	740 ± 37	555 ± 28	1295 ± 65	5.59 ± 0.40	2.17 ± 0.17	4.12 ± 0.30	-	1410 ± 70
Obi-DSS-25 m	Am-06-57	0.325	0.1117	2920 ± 125	935 ± 58	3855 ± 180	670 ± 40	390 ± 19	1060 ± 60	6.53 ± 0.48	3.59 ± 0.29	5.45 ± 0.40	410 ± 35	1340 ± 67
Obi-DSS-40 m	Am-06-56	0.308	0.0998	2980 ± 125	710 ± 49	3690 ± 175	685 ± 34	370 ± 18	1055 ± 53	6.51 ± 0.42	2.89 ± 0.25	5.25 ± 0.36	-	1500 ± 75
Obi-DSS-55 m	Am-06-55	0.214	0.1354	2200 ± 110	720 ± 45	2920 ± 160	470 ± 28	280 ± 14	750 ± 42	6.99 ± 0.55	3.88 ± 0.31	5.84 ± 0.45	280 ± 25	1110 ± 56
Depth-integrated value[d]:		0.25		2300	750	3190	552	339	890	6.24	3.31	5.36		1230
Madeira Depth Profile (Sampled in 2006; Mean Depth-Integrated Grain Size [D90] = 62 μm)														
Mad-DSS-0 m	Am-06-35	0.395	0.1139	2660 ± 115	1065 ± 60	3730 ± 175	780 ± 47	520 ± 26	1300 ± 73	5.11 ± 0.38	3.07 ± 0.23	4.30 ± 0.31	370 ± 35	1890 ± 94
Mad-DSS-6 m	Am-06-34	0.288	0.1096	2000 ± 92	710 ± 49	2700 ± 140	600 ± 36	435 ± 22	1035 ± 58	4.97 ± 0.38	2.43 ± 0.21	3.90 ± 0.30	240 ± 25	1550 ± 77
Mad-DSS-12 m	Am-06-33	0.222	0.1400	1660 ± 80	635 ± 41	2295 ± 120	490 ± 29	360 ± 18	850 ± 47	5.08 ± 0.39	2.61 ± 0.21	4.03 ± 0.31	150 ± 17	1330 ± 66
Depth-integrated value[d]:		0.34		2340	1047	3230	688	474	1160	5.09	3.31	4.16		1710

[a]All uncertainties denote 1σ analytical uncertainties. For stable ^{9}Be measurements using ICP-OES, a 5% error is propagated into ^{10}Be/^{9}Be ratios. For ^{10}Be measurements, a blank ratio of $6.3 \pm 3.8 \times 10^{-16}$ ($n = 4$) was subtracted, and the error was propagated into ^{10}Be concentrations. All suspended sediment data were measured at Cologne AMS. Sampling was carried out according to *Bouchez et al.* [2011a], involving onboard separation from water phase using 0.22 μm filter sheets.

[b]These samples were also analyzed by *Bouchez et al.* [2010, 2011a].

[c]Al/Si data for the Madeira and Amazon are from *Bouchez et al.* [2011b].

[d]Concentrations were calculated using linear regression and Al/Si depth-integrated value; corresponding ratios were calculated from depth-integrated concentrations. No error propagation was carried out; uncertainties are likely high due to two-point correlations in some cases.

Table 4. Meteoric ^{10}Be, ^{9}Be, and ^{10}Be/^{9}Be Ratio Data for River Water Samples

Sample[a]	Original Sample Code	Initial Water Weight for ^{10}Be Analysis (g_{water})	Initial Water Weight for ^{9}Be Analysis (g_{water})	$[^{10}Be]_{diss}$ (at/g_{water})	$[^{9}Be]_{diss}$ ($\times 10^{-12}$ g/g_{water})	$(^{10}Be/^{9}Be)_{diss}$ ($\times 10^{-10}$)
Be1-W[b]	AM 01-14	549.3	69.21	156 ± 67	3.69 ± 0.02	6.3 ± 2.7
Md15-W[b]	AM 01-15	724.6	59.61	148 ± 60	4.59 ± 0.02	4.8 ± 2.0
Ir-W[b]	AM 06/1-07	573.3	66.60	1150 ± 144	19.39 ± 0.10	8.9 ± 1.1
Par-W[b]	AM 06/1-10	733.4	64.23	1360 ± 105	22.81 ± 0.11	8.93 ± 0.69
Obi-W[b]	AM 06-63	503.7	69.91	1020 ± 154	20.20 ± 0.10	7.5 ± 1.1
Mad-W1[b]	AM 06/1-03	619.7	66.85	549 ± 104	12.70 ± 0.06	6.5 ± 1.2
Mad-W2[c]	AM 06/1-03	359.6	-	568 ± 52	-	6.70[d] ± 0.61
Ne-W[c]	AM 06/1-02	795.4	See Brown et al.	6220 ± 232	21.72[e] ± 0.11	43 ± 12

[a]All uncertainties denote 1σ analytical uncertainties. For ^{10}Be measurements, a blank ratio of $1.75 \pm 0.07 \times 10^{-15}$ ($n = 2$) was subtracted, and error was propagated into ^{10}Be concentration. All water ^{10}Be data were measured at ETH Zurich, except Ne-W and Mad-W2 (Cologne AMS). Approximately equal volumes of water were sampled at the same depths as suspended sediments and were composited to a final volume of 2 L, filtered using 0.22 μm filter sheets, then acidified to a pH of 1–2, and stored and refrigerated upon arrival in the lab.
[b]Processed in 2012 and measured at ETH AMS.
[c]Processed in 2013 and measured at Cologne AMS, where Mad-W2 is a replicate of Mad-W1 (processed in two different labs by two operators). Note that their $[^{10}Be]$ values agree within 1 σ analytical uncertainty.
[d]Calculated using $[^{9}Be]$ of sample Mad-W1.
[e]Value is from *Brown et al.* [1992].

substantial amounts of sediment, the main portion of erosion is captured when using floodplain-corrected denudation rates (D_insitu_{FP}). When multiplying D_insitu_{FP} with the respective sediment-producing areas, approximately 600 Mt/yr of sediment can be calculated to reach the sea, a number that compares well to a mean of approximately 1000 Mt/yr from a modern, gauging-derived sediment budget [*Wittmann et al.*, 2011a]. The difference between these two estimates is attributed to differences in integration time scale (kyr for in situ versus several years for gauging-derived fluxes, respectively).

3. Methods

3.1. Analytical Methods

Solid samples (bed load and suspended sediment from depth profiles) were weighed (Tables 2 and 3) and the leaching procedure of *Wittmann et al.* [2012] was applied under clean lab conditions (see *Wittmann et al.* [2012] for full procedure), yielding reactive fractions. Splits from these fractions were analyzed for stable ^{9}Be concentrations by Inductively Coupled Plasma-Optical Emission Spectroscopy (ICP-OES) and cosmogenic ^{10}Be concentrations by Accelerator Mass Spectrometry (AMS) after spiking with a ^{9}Be carrier and chromatographic separation of pure Be. Water samples were separated into two samples, where one subsample was used for sector field High-Resolution Inductively Coupled Plasma-Mass Spectrometry (HR-ICP-MS) for ^{9}Be analysis and another was used for ^{10}Be analysis by AMS after spiking with a ^{9}Be carrier and separation of Be (Table 4). A $FeCl_3$ solution was added to the AMS sample portions to coprecipitate Be with ferric hydroxide (an approach adapted from *Jeandel* [1993] and *Frank et al.* [2009] developed for ocean water). The full analytical procedures are given in sections S2 and S3 in the supporting information; we also conducted Be yield tests of the water precipitation method.

3.2. Basin-Wide Depositional ^{10}Be Fluxes

The ECHAM5-GCM with the HAM aerosol module [*Heikkilä et al.*, 2013a, 2013b] describes atmospheric transport and deposition of meteoric ^{10}Be averaged over three 11 year solar cycles with a spatial resolution of 2.8° by 2.8° and has a higher vertical resolution than the GISS-GCM [*Field et al.*, 2006]. For an assessment of the climate-induced differences in meteoric ^{10}Be deposition over time, two published deposition model runs were combined [*Heikkilä and von Blanckenburg*, 2015]. A modern ("industrial") model run of ^{10}Be deposition, using present-day atmospheric conditions and aerosol loading [*Heikkilä et al.*, 2013a], was combined with an early Holocene ("preindustrial") model run [*Heikkilä et al.*, 2013b], using preindustrial aerosol and greenhouse gas conditions. For both models, the modern solar modulation constant Φ of 501.76 MV [*Heikkilä et al.*, 2013a] was rescaled to an average Holocene Φ of 280.94 MV derived from the average common production rate [*Steinhilber et al.*, 2012] that includes changes in Φ and geomagnetic field changes. The modern and the preindustrial model runs were combined by averaging [*Heikkilä and von Blanckenburg*, 2015]. The average area-weighted global

Table 5. Depositional ^{10}Be Fluxes and ^{10}Be Mass Balance[a]

Sample	F_{met}^{10Be} Basin-Wide Depositional Flux[b] ($\times 10^6$ at/cm^2/yr)	F_{met}^{10Be} Depositional Flux for Andean Area[c] ($\times 10^6$ at/cm^2/yr)	J_{atm}^{10Be} ($\times 10^{20}$ at/yr)	J_{riv}^{10Be} (Gauging)[d] ($\times 10^{20}$ at/yr)	J_{riv}^{10Be} (In Situ)[d] ($\times 10^{20}$ at/yr)	$\frac{J_{riv}^{10Be}}{J_{atm}^{10Be}}$ (Gauging)[e]	$\frac{J_{riv}^{10Be}}{J_{atm}^{10Be}}$ (In Situ)[f]
Be 1 (average)	2.10 ± 0.17	2.10	14.2	16.1	5.06	1.14 ± 0.54	0.36 ± 0.18
Be-DSS	2.10 ± 0.17	2.10	14.2	38.5	12.0	2.7 ± 1.3	0.85 ± 0.42
Be 2-1	2.10 ± 0.17	2.10	15.3	13.2	7.61	0.86 ± 0.41	0.50 ± 0.26
Be 2-2	2.10 ± 0.17	2.10	15.3	11.6	6.66	0.76 ± 0.36	0.43 ± 0.22
Be 3	2.10 ± 0.17	2.10	16.9	12.2	4.67	0.73 ± 0.34	0.28 ± 0.13
Be 4	2.21 ± 0.18	2.10	20.5	12.7	2.31	0.62 ± 0.29	0.113 ± 0.054
Be 8	2.21 ± 0.18	2.10	24.3	9.54	3.26	0.39 ± 0.19	0.134 ± 0.064
Be 10	2.21 ± 0.18	2.10	25.0	10.9	3.18	0.44 ± 0.21	0.127 ± 0.060
Be 12	2.21 ± 0.18	2.10	27.3	6.86	3.58	0.25 ± 0.12	0.131 ± 0.071
Md 15	1.83 ± 0.05	1.83	25.6	5.65	4.16	0.22 ± 0.10	0.16 ± 0.10
Md-DSS	1.83 ± 0.05	1.83	25.6	17.8	13.0	0.70 ± 0.31	0.51 ± 0.33
OR 16	1.44 ± 0.42	1.44	4.60				
Be 17	2.07 ± 0.12	2.10	63.1	11.8	4.52	0.186 ± 0.088	0.072 ± 0.035
Mar 18	1.96 ± 0.22	2.43	118				
Mad 19	2.05 ± 0.21	1.96	181				
Mad 20	1.98 ± 0.20	1.96	189				
GR 19	1.96 ± 0.42	1.96	11.7				
Pe 101	0.824 ± 0.081	0.68	60.5				
Pe 107	0.92 ± 0.12	0.83	33.2				
Man 2.4[g]	1.17 ± 0.10	0.75	266	85.5	52.6	0.321 ± 0.078	0.197 ± 0.048
Ir 1.75	1.19 ± 0.11	0.75	376	235	136	0.62 ± 0.15	0.363 ± 0.087
Par 0.9	1.42 ± 0.14	1.30	672	255	136	0.380 ± 0.085	0.202 ± 0.046
Par 1.2	1.42 ± 0.14	1.30	672	152	90.6	0.226 ± 0.050	0.135 ± 0.030
Par 1.6	1.42 ± 0.14	1.30	672	124	78.5	0.185 ± 0.041	0.117 ± 0.026
Par 2.2	1.42 ± 0.14	1.30	672	258	137	0.384 ± 0.084	0.204 ± 0.045
Obi (average)	1.39 ± 0.14	1.30	706	193	126	0.274 ± 0.070	0.179 ± 0.046
Obi-DSS	1.39 ± 0.14	1.30	706	354	209	0.62 ± 0.16	0.36 ± 0.10
Mad 0.3	1.83 ± 0.19	1.96	264	109	41.8	0.41 ± 0.11	0.158 ± 0.044
Mad 0.5	1.83 ± 0.19	1.96	264	51.3	21.6	0.195 ± 0.054	0.082 ± 0.023
Mad 1.8	1.83 ± 0.19	1.96	264	310	112	1.18 ± 0.32	0.43 ± 0.12
Mad-DSS	1.83 ± 0.19	1.96	264	146	54.5	0.55 ± 0.15	0.207 ± 0.058
Cb 2 (average)	1.44 ± 0.18	1.44	15.8				
Cb 3	1.52 ± 0.19	1.52	3.05				
Cb 5	1.32 ± 0.25	1.32	1.61				
Cb 6	1.09 ± 0.26	1.09	10.2				
Br 2	1.03 ± 0.19	1.03	15.0				
Br 3	1.03 ± 0.19	1.03	13.7				
Br 4	1.03 ± 0.19	1.03	15.5				
Br 7 (average)	1.03 ± 0.15	1.03	21.8				
Ne 0.6	1.160 ± 0.082	1.16	96.5	56.0	56.4	0.58 ± 0.12	0.58 ± 0.11

[a](1) For DSS data, we used depth-integrated ^{9}Be and ^{10}Be concentrations for all calculations and (2) $J_{10Be\text{-}riv}$ and $J_{10Be\text{-}riv}/J_{10Be\text{-}atm}$ derived from bed load data are biased by grain size effects.

[b]Basin-wide meteoric ^{10}Be flux calculated for each basin (on SRTM-derived pixel basis) using an average of industrial and preindustrial model runs [*Heikkilä et al*., 2013a, 2013b]. Uncertainty is the difference between two runs.

[c]Meteoric ^{10}Be flux calculated for Andean area of each basin (on SRTM-derived pixel basis using the area $>$ 350 m elevation) using an average of industrial and preindustrial model runs [*Heikkilä et al*., 2013a, 2013b]. Uncertainty is assumed to be similar to basin-wide flux.

[d]Calculated using equation (3) and gauging- or in situ-derived sediment fluxes. Where reasonable, we used dissolved data from other samples as approximation (e.g., Be-W was used for all Beni trunk stream samples). For Cb and Br samples, no $[^{10}Be]_{diss}$ is available and cannot be approximated, and for Cb, no gauging loads are available.

[e]Error calculated by propagating all 1σ analytical uncertainties for [^{10}Be], a 10% uncertainty on water discharge and sediment gauging data, and the uncertainty given for $F_{10Bemet}$.

[f]Error calculated by propagating all 1σ analytical uncertainties for [^{10}Be], a 10% uncertainty on water discharge, the uncertainty given in Table 1b for in situ-derived denudation rates, and the uncertainty given for $F_{10Bemet}$.

[g]For calculations we used a $[^{10}Be]_{diss}$ of 385 at/g$_{water}$ that was taken from *Brown et al*. [1992].

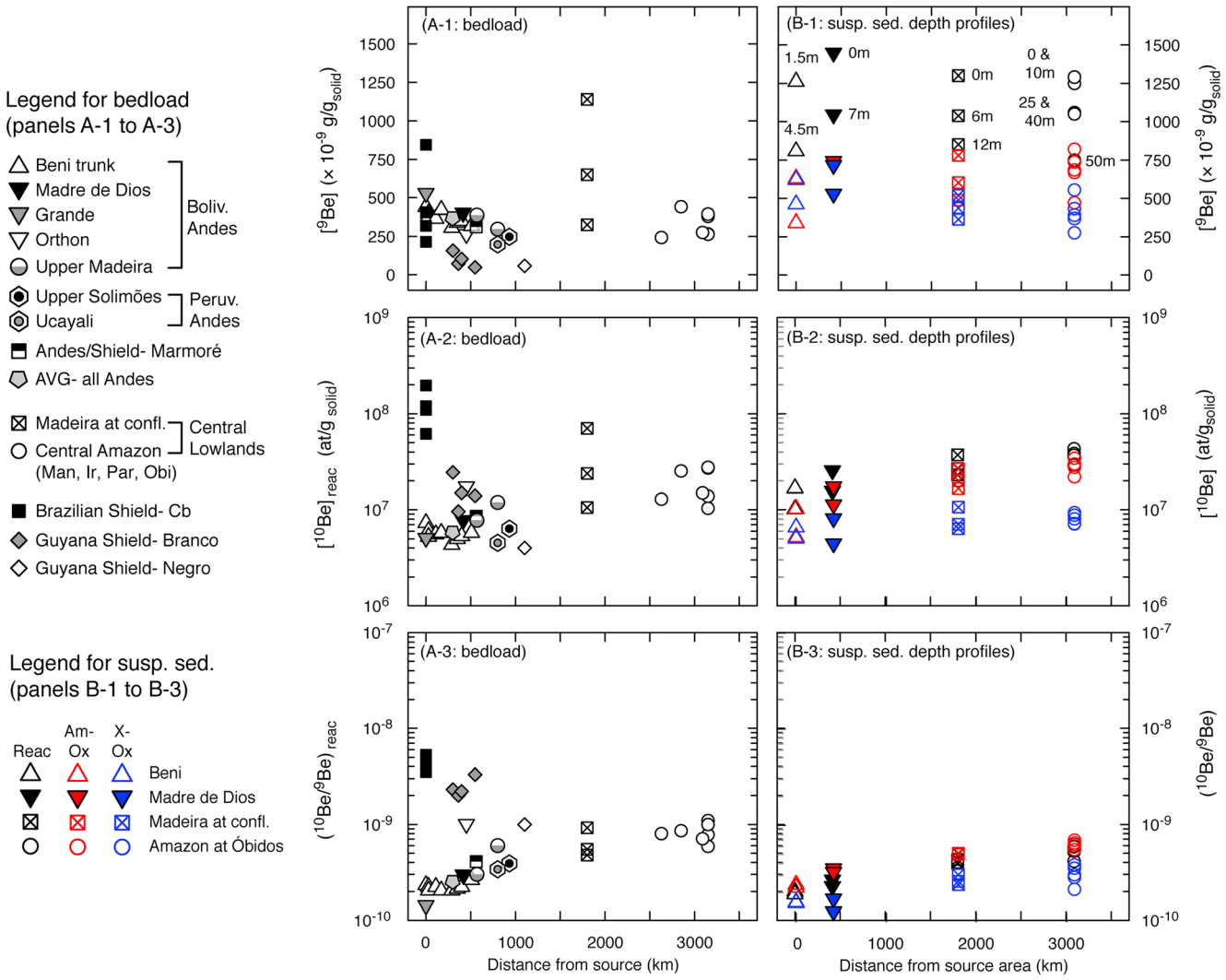

Figure 2. (A-1 to A-3) $[^{9}Be]_{reac}$ ($\times 10^{-9}$ g/g_{solid}), $[^{10}Be]_{reac}$ (at/g_{solid}) and ($^{10}Be/^{9}Be$) ratios for bed load samples; (B-1 to B-3) same quantities for suspended sediment samples from depth profiles. Water depth is given next to samples from depth profiles for Figure 2B-1. Blue and red symbols indicate am-ox (amorphous oxide leach) and x-ox (crystalline oxide leach) extracted fractions that comprise the total reactive fraction given in black.

flux in both models is 1.09×10^{6} $at/cm^2/yr$. Longitude- and latitude-based $F^{^{10}Be}_{met}$ (Table 5) were then calculated for each subbasin from this average model using digital elevation model (DEM) software. As an uncertainty intrinsic to these two modeling approaches, we propagated the relative difference between the two model runs into all calculations (Table 5). This difference represents the maximum possible variation within the given accuracy of known transport and deposition models and typically amounts to no more than 20% at the basin scale (see link to distribution maps of *Heikkilä and von Blanckenburg* [2015], before the Acknowledgements).

4. Results

4.1. Meteoric ^{10}Be Concentrations, Stable ^{9}Be Concentrations, and $^{10}Be/^{9}Be$ Ratios of Bed Load

The $[^{10}Be]_{reac}$ in the bed load of Andean rivers averages to 560×10^{4} at/g_{solid} (for uncertainties, see Table 2), while samples from the central Amazon lowlands average from 1900×10^{4} at/g_{solid} (samples Man, Ir, Par, Obi, see Figure 1) to 3500×10^{4} at/g_{solid} for the lower Madeira (Figure 2A-2). In the upper Guyana Shield (Branco), $[^{10}Be]_{reac}$ is 1600×10^{4} at/g_{solid}. In the lower Guyana Shield, we measured one bed load sample from the Negro, which yielded low $[^{10}Be]_{reac}$ of 400×10^{4} at/g_{solid}. Note that for these samples from the Branco and Negro, coarse bed load was leached in the absence of fine material. In the upper Brazilian Shield, an average

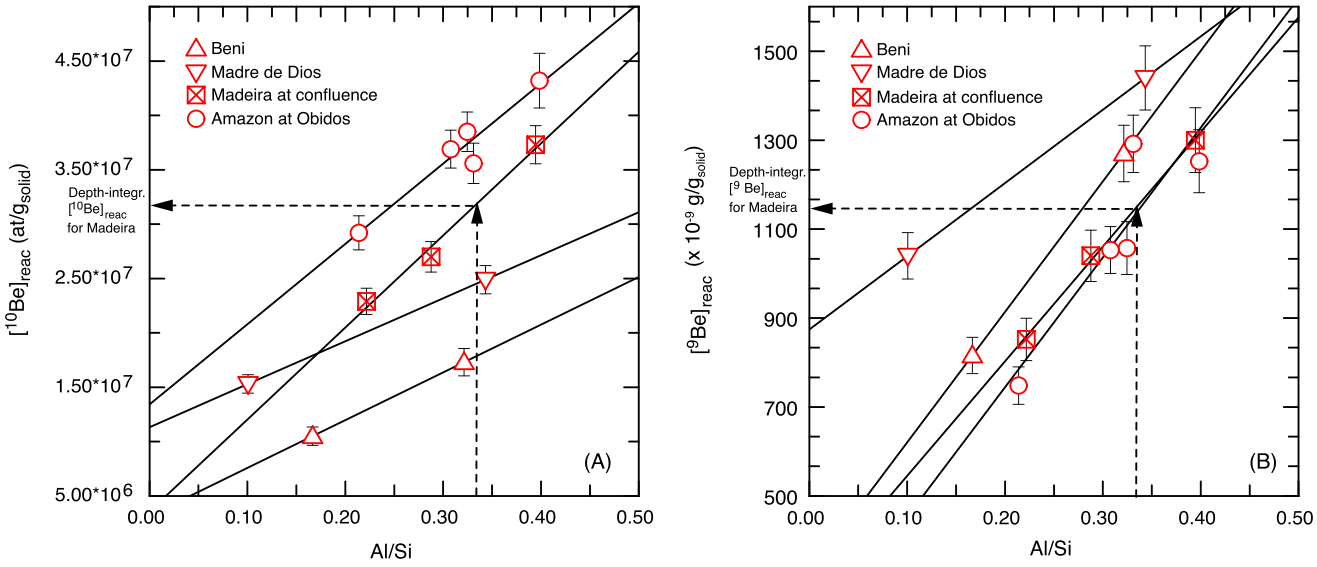

Figure 3. (a) $[^{10}Be]_{reac}$ (at/g_{solid}) versus Al/Si ratio and (b) $[^{9}Be]_{reac}$ ($\times 10^{-9}$ g/g_{solid}) versus Al/Si ratio for suspended sediment depth profiles (DSS). A depth-integration of $[^{10}Be]_{reac}$ and $[^{9}Be]_{reac}$ is from linear regression for each river data set (see example shown for the Madeira with the arrows). Similar trends are found between $[^{9}Be]_{min}$ and Al/Si ratios (not shown). Resulting depth-integrated values are shown from hereon in red.

bed load $[^{10}Be]_{reac}$ is $12{,}000 \times 10^4$ at/g_{solid}. Meteoric ^{10}Be concentrations of the silicate residue ($[^{10}Be]_{min}$) are usually <10% of the total bed load $[^{10}Be]$ ($[^{10}Be]_{total}$, sum of $[^{10}Be]_{min}$ and $[^{10}Be]_{reac}$), such that the majority of $[^{10}Be]_{total}$ is contributed by reactive ^{10}Be. The exception is the Branco River, for which the average $[^{10}Be]_{min}$ comprises 35% of the bed load $[^{10}Be]_{total}$ (Table 2).

For ^{9}Be in bed load samples (Table 2), only 18–37% was found in the reactive ^{9}Be fraction. The average bed load $[^{9}Be]_{reac}$ for all the Andes is 360×10^{-9} g/g (Figure 2A-1), and the average bed load $[^{9}Be]_{reac}$ for the entire central Amazon is 330×10^{-9} g/g. Therefore, $[^{9}Be]_{reac}$ in bed load does not vary strongly across the basin from the Andes to the central lowlands.

The lowest $(^{10}Be/^{9}Be)_{reac}$ ratios in bed load are found in the Andes (Figure 2A-3) with $(^{10}Be/^{9}Be)_{reac} = 2.5 \times 10^{-10}$. In bed load of the central Amazon lowlands, significantly higher ratios of 8.4×10^{-10} are found. However, the highest basin-wide bed load $(^{10}Be/^{9}Be)_{reac}$ ratios were found in the shields (24.9×10^{-10} in the upper Guyana Shield, 10.4×10^{-10} in the Negro, and 43.7×10^{-10} in the Brazilian Shield).

4.2. Meteoric ^{10}Be Concentrations, Stable ^{9}Be Concentrations, and $^{10}Be/^{9}Be$ Ratios of Suspended Sediments From Depth Profiles

For suspended sediment depth profiles (DSS), $[^{10}Be]_{reac}$ (Table 3 and Figure 2B-2) varies within a factor of 2 with sampling depth. $[^{10}Be]_{reac}$ in suspended sediment (Table 3) increases from the Andes to the Amazon lowlands, from approximately 2000×10^4 at/g_{solid} to 3200×10^4 at/g_{solid}, respectively. For these DSS samples, the $[Be]_{am\text{-}ox}$ (amorphous oxides of the reactive phase) and the $[Be]_{x\text{-}ox}$ (crystalline oxides of the reactive phase) fractions were measured separately (Table 3). Importantly, $[^{10}Be]_{am\text{-}ox}$ is a factor of 1.5 to 2 times higher than $[^{10}Be]_{x\text{-}ox}$ in the suspended sediment of Andean rivers, and between a factor of 2 to 4 times higher in the suspended sediment of lowland rivers (Table 3). The $[^{10}Be]_{min}$, measured for the Madeira and Óbidos depth profiles, comprises <10% of the suspended sediment $[^{10}Be]_{total}$, with the am-ox fraction comprising approximately 65–72% of $[^{10}Be]_{total}$.

In comparison, $[^{9}Be]_{reac}$ shows larger variability with depth in the river than $[^{10}Be]_{reac}$ (compare Figures 2B-1 and 2B-2). However, the distribution of am-ox and the x-ox fractions of ^{9}Be in suspended sediment is more uniform than that of $[^{10}Be]_{reac}$ for the different geomorphic zones. For Andean rivers, the $[^{9}Be]_{am\text{-}ox}$ fraction in suspended sediment is roughly equal to the $[^{9}Be]_{x\text{-}ox}$ fraction, and in the Madeira and main Amazon, suspended sediment $[^{9}Be]_{am\text{-}ox}$ is only slightly higher by a factor of 1.3 to 2 than $[^{9}Be]_{x\text{-}ox}$ (Table 3). Around 60% of $[^{9}Be]_{total}$ in the suspended sediment was found in the silicate residue fraction. Both $[^{9}Be]_{reac}$ (ranging

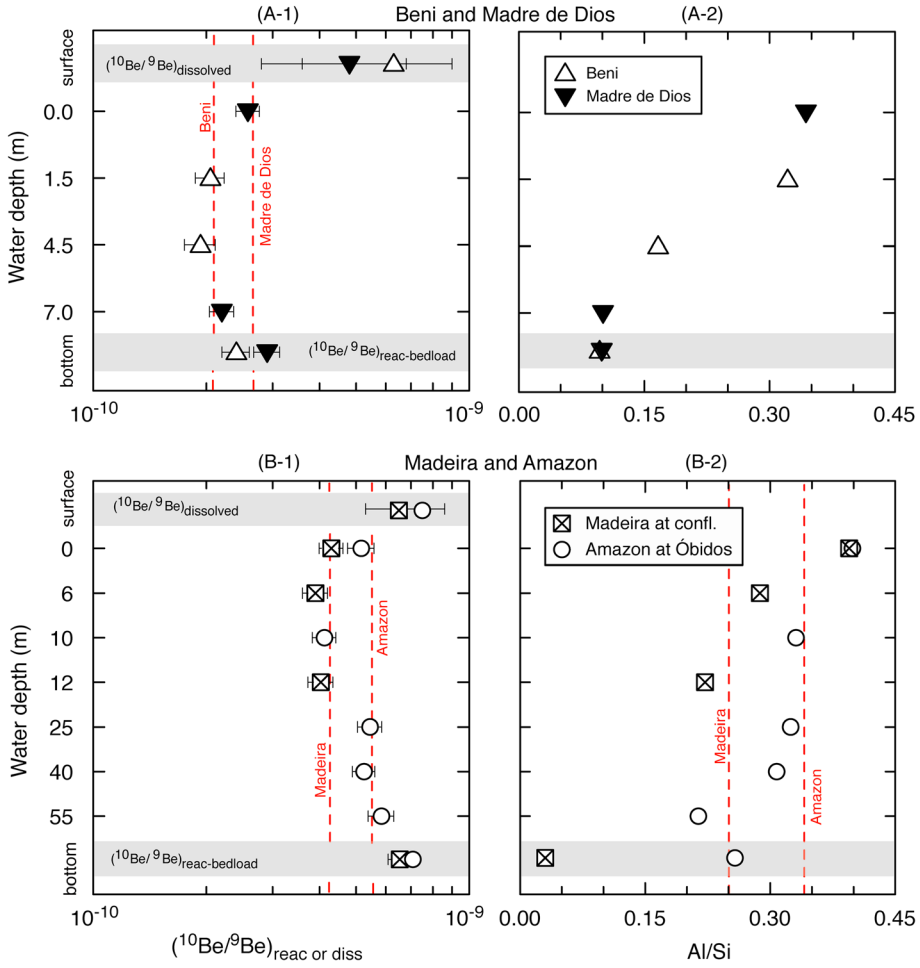

Figure 4. Depth profiles of suspended sediment samples of (top row) the Beni and Madre de Dios and (bottom row) the Madeira at its confluence and Amazon at Óbidos; (A-1 and B-1) $(^{10}Be/^{9}Be)_{reac}$ and (A-2 and B-2) Al/Si (measured by *Bouchez et al.* [2011b]) (Table 3). In Figures 4A-1 and 4B-1, $(^{10}Be/^{9}Be)_{reac}$ from bed load (Table 2) and $(^{10}Be/^{9}Be)_{diss}$ (Table 4) are shown for comparison. Red stippled lines represent depth-integrated DSS-$(^{10}Be/^{9}Be)_{reac}$ and Al/Si as in Figure 3. A depth integrated Al/Si ratio is not available for the Beni and Madre de Dios rivers (Figure 4A-2).

from approximately 1000 to 1200×10^{-9} g/g) and $[^{9}Be]_{min}$ (average of approximately 2500×10^{-9} g/g) are higher in suspended sediment than in bed load (compare Figures 2A-1 and 2B-1).

We find higher mean $[^{9}Be]_{min}$ in suspended sediments than in bed load. Indeed, X-ray diffraction detected minerals like illite that can incorporate Be, whereas bed load samples are mainly composed of quartz and feldspar (supporting information section S4). However, a characterization of reactive phases by major elemental analysis relative to total elemental concentrations ([Element X]$_{reac}$ / [Element X]$_{total}$) shows similar trends for bed load and suspended sediment samples (section S5 in the supporting information). This similarity implies that the contribution of the reactive phase relative to the bulk elemental budget does not depend too strongly on grain size.

For both $[^{10}Be]_{reac}$ and $[^{9}Be]_{reac}$ measured along the suspended sediment depth profiles, we find a significant correlation with the Al/Si ratio (Figure 3). The Al/Si ratio is a substitute for grain size, with low ratios reflecting coarse, quartz-rich sediment, and higher values characteristic of finer, clay-rich sediment [*Bouchez et al.*, 2011a]. This correlation implies a dependence of $[^{10}Be]_{reac}$ on particle size that was found in previous studies [*Gu et al.*, 1996; *Shen et al.*, 2004; *Wittmann et al.*, 2012] and is mostly due to dilution of absolute concentrations by quartz in coarse-grained samples. In order to correct for this grain size effect, we use the observed correlation between Al/Si and $[^{10}Be]_{reac}$ and $[^{9}Be]_{reac}$ shown in Figure 3, together with the grain size-integrated Al/Si ratios of 0.25 for the Solimões and 0.34 for the Madeira calculated by *Bouchez et al.* [2011b]. These ratios were estimated by depth integration of suspended sediment chemistry along depth

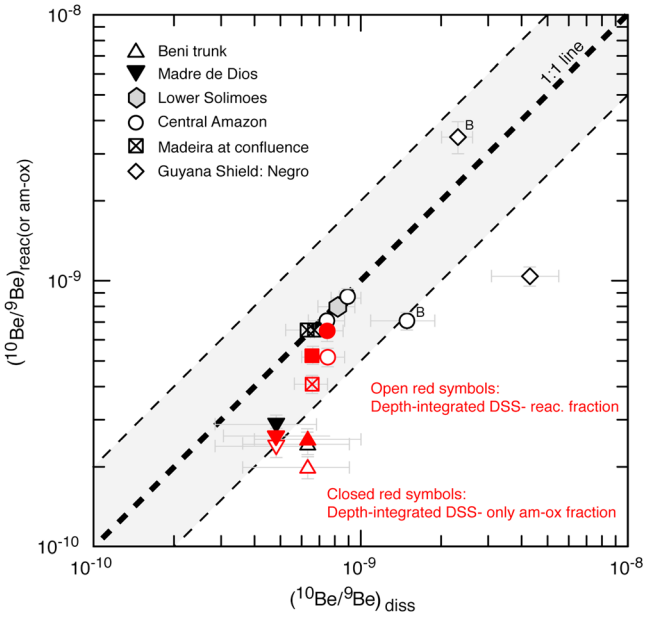

Figure 5. $(^{10}Be/^{9}Be)_{diss}$ (Table 4) for the Amazon basin versus (i) $(^{10}Be/^{9}Be)_{reac}$ from bed load samples (black symbols, Table 2), (ii) $(^{10}Be/^{9}Be)_{reac}$ from depth-integrated suspended sediment (DSS, open red symbols, Table 3), and (iii) $(^{10}Be/^{9}Be)_{am\text{-}ox}$ from DSS (closed red symbols, Table 3). $(^{10}Be/^{9}Be)_{x\text{-}ox}$ for DSS samples are not shown but note that these would plot below the "reac" open red symbols in vertical direction farther away from the 1:1 line. Grey stippled area gives the factor-of-2 range around the 1:1 line between $(^{10}Be/^{9}Be)_{reac}$ and $(^{10}Be/^{9}Be)_{diss}$ ratios. Some values are from *Brown et al.* [1992], (labeled "B").

profiles obtained during two river sampling campaigns performed at distinct hydrological conditions. The depth-integrated $[^{10}Be]_{reac}$ and $[^{9}Be]_{reac}$ thereby obtained (Figure 3) are representative of reactive Be concentrations in bulk suspended sediment carried by the Amazon and Madeira Rivers. In the absence of grain size-integrated chemical composition data for the smaller Beni and Madre de Dios rivers, we use the Madeira's Al/Si value of 0.34 for these rivers, as the Beni and Madre de Dios are Madeira tributaries draining similar source rocks. The depth-integrated $[^{10}Be]_{reac}$, $[^{9}Be]_{reac}$, and $(^{10}Be/^{9}Be)_{reac}$ for each of the suspended sediment depth profiles are given in Table 3 and are used for all calculations to follow (flux-based mass balance, erosion, and denudation rates) rather than a mere average of all suspended sediment samples. The depth-integrated DSS-$(^{10}Be/^{9}Be)_{reac}$, shown here in red and in all subsequent figures, are all systematically lower than $(^{10}Be/^{9}Be)_{reac}$ of bed load but agree within a factor of approximately 2 (Figures 3 and 4).

4.3. Water Samples: $[^{10}Be]_{diss}$, $[^{9}Be]_{diss}$, and $(^{10}Be/^{9}Be)_{diss}$

Andean rivers have the lowest $[^{10}Be]_{diss}$, with 150 at/g_{water}, while values in lowland rivers range between 550 and 1360 at/g_{water} (Table 4 and Figure S2 in the supporting information). The Negro River has the highest $[^{10}Be]_{diss}$ of 6215 at/g_{water}. These concentrations are comparable to those obtained by *Brown et al.* [1992]. Similarly, $[^{9}Be]_{diss}$ of Andean rivers are lowest with $3.7–4.6 \times 10^{-12}$ g/g_{water}. Concentrations of the main Amazon River and the Madeira are an order of magnitude higher ($12.7–22.8 \times 10^{-12}$ g/g_{water}). These values are similar to those from *Brown et al.* [1992].

Ratios of $(^{10}Be/^{9}Be)_{diss}$ are 4.8×10^{-10} and 6.3×10^{-10} in Andean rivers and 6.5×10^{-10} to 8.9×10^{-10} in lowland rivers (Figure 5), with the exception of the Negro, which yields a $(^{10}Be/^{9}Be)_{diss}$ of 4.3×10^{-9}. The $^{10}Be/^{9}Be_{diss}$ ratios obtained by *Brown et al.* [1992] were 8.2×10^{-10} for the Solimões at Manaus, 1.5×10^{-9} for the Amazon at Macapa, and 2.3×10^{-9} for the Negro [*Brown et al.*, 1992].

4.4. $(^{10}Be/^{9}Be)_{reac}$ Versus $(^{10}Be/^{9}Be)_{diss}$ Ratios and $(^{10}Be/^{9}Be)_{am\text{-}ox}$ Versus $(^{10}Be/^{9}Be)_{diss}$

We can now compare the $^{10}Be/^{9}Be$ ratio carried by the reactive fraction of bed load and suspended sediments with that carried in dissolved form in river water. A very good correlation is observed between $(^{10}Be/^{9}Be)_{reac}$ from bed load samples and $(^{10}Be/^{9}Be)_{diss}$ ratios for the large Amazon and Madeira rivers (Figure 5). Slightly more scatter is observed for smaller tributaries such as the Beni and the Madre de Dios rivers, but values agree within a factor of about 2 (grey stippled area in Figure 5). For the Negro River, the two independent estimates by *Brown et al.* [1992] and this study, respectively, do not agree but are offset in opposite directions by a factor of 1.5 and approximately 4, respectively, from the 1:1 line of equal reactive versus dissolved ratios (Figure 5).

Depth-integrated $(^{10}Be/^{9}Be)_{reac}$ ratios of DSS samples (Figure 5, open red symbols) differ from $(^{10}Be/^{9}Be)_{diss}$ more significantly than bed load-derived $(^{10}Be/^{9}Be)_{reac}$. For the Beni, this observation could be explained by the fact that bed load was sampled in a different year than suspended sediment and water (supporting information

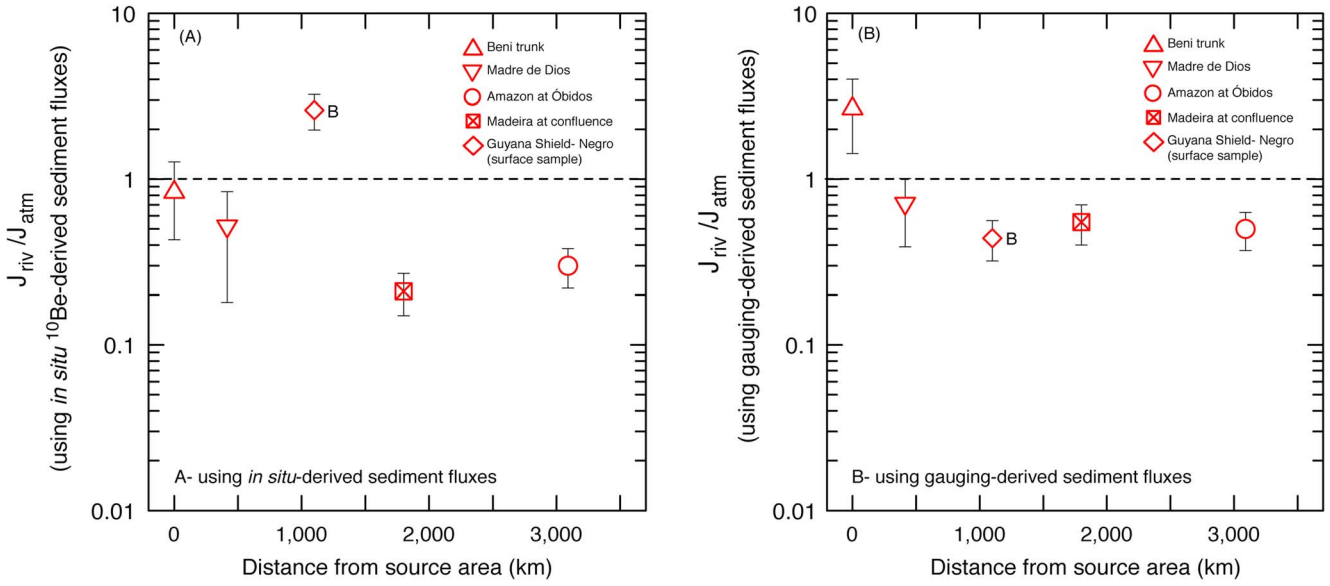

Figure 6. (a) Ratio of basin-wide sedimentary ^{10}Be export (J_{riv}^{10Be}) versus basin-wide ^{10}Be deposition (J_{atm}^{10Be}, Table 5). J_{riv}^{10Be} was calculated using in situ ^{10}Be-derived sediment fluxes from D_insitu$_{FP}$ and [^{10}Be]$_{reac}$ from depth-integrated suspended sediment (for Negro surface suspended sediment was used, indicated by B [see *Brown et al.*, 1992]). (b) Same ratio using gauging-derived sediment fluxes versus J_{atm}^{10Be}. Uncertainties include 1σ analytical uncertainties, the uncertainty given in Table 5 for basin-specific F_{met}^{10Be}, a 10% uncertainty on water discharge and gauging-derived sediment flux, or the uncertainty given in Table 1b for in situ-derived D_insitu$_{FP}$, respectively. Note that a difference between the in situ- versus gauging-derived J_{riv}^{10Be} is expected due to differences in integration time scale (approximately 10 yr for gauging versus several kiloyears for in situ-derived sediment fluxes; section 2.2 [*Wittmann et al.*, 2011a]).

section S1). Interestingly, however, depth-integrated DSS-(^{10}Be/^{9}Be)$_{am\text{-}ox}$ (Table 3 and Figure 5, closed red symbols) agree better with (^{10}Be/^{9}Be)$_{diss}$ than corresponding DSS-(^{10}Be/^{9}Be)$_{reac}$ (section 5.2).

5. Discussion of ^{10}Be and ^{9}Be Concentrations and ^{10}Be Fluxes

5.1. A Flux Balance for ^{10}Be

We have calculated a flux balance for ^{10}Be that is based on equations (1)–(4). With this balance we can test whether the atmospheric flux estimated from cosmogenic nuclide production models combined with global circulation models on the one hand and the sedimentary flux estimated from river loads and [^{10}Be] on the other hand are at steady state in the Amazon basin. This mass balance approach is similar to the one presented in *Granger et al.* [2013] for meteoric ^{10}Be in basins of the Eastern United States measured by *Brown et al.* [1988]. For our mass balance, we rely on [^{10}Be]$_{reac}$ from depth-integrated DSS samples that we consider representative in [^{10}Be]$_{reac}$ with respect to grain size and sorting effects (section 4.2).

Two different estimates of this flux balance are shown in Figure 6. The erosion rate E_i, which is the input quantifying the sedimentary flux (equation (3)) is either derived from modern sediment loads or from longer-term D_insitu$_{FP}$ (Table 1b). D_insitu$_{FP}$ is the floodplain-corrected denudation rate [*Wittmann et al.*, 2011a] calculated under the assumption that all sediment is eroded from the mountains and that production of further in situ cosmogenic nuclides is negligible in the floodplain. Note that when using D_insitu$_{FP}$, the derived sediment fluxes provide an upper limit as they include a weathering component, because in situ denudation rates integrate over all weathering and erosion processes.

We first note that the relative exported sedimentary ^{10}Be flux ratio $J_{riv}^{10Be}/J_{atm}^{10Be}$ is mostly lower than 1 (Figure 6). If a deficit is present, it amounts to approximatley 20–85% of the meteoric flux deposited into the basin (Table 5). If we assume that this deficit does not arise from the dissolved flux, which is negligible in the mainstream due to the near-neutral pH, this deviation from the steady state case may have several causes.

1. An overestimate of F_{met}^{10Be} in equation (1) might result in observed $J_{riv}^{10Be}/J_{atm}^{10Be} < 1$. Indeed, our entire approach relies upon the accuracy of the GCM-derived depositional flux. We regard it as likely that on

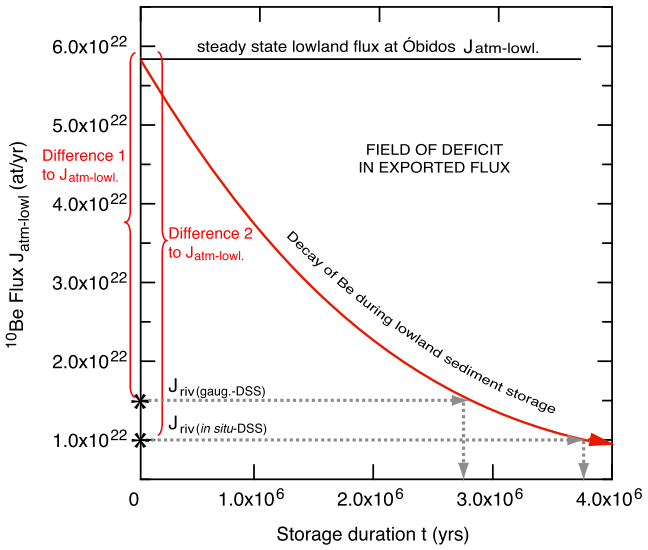

Figure 7. The storage duration t (in Myr) required to reduce the riverine flux of ^{10}Be in the lowlands at Óbidos, $J_{riv\text{-}lowl}$, relative to the depositional flux onto the floodplain upstream of Óbidos ($J^{^{10}Be}_{atm\text{-}lowl}$; horizontal black line). "$J^{^{10}Be}_{riv}$ (gauging-DSS)" denotes "difference 1" between $J^{^{10}Be}_{atm\text{-}lowl}$ and the $J^{^{10}Be}_{riv\text{-}lowl}$ using a gauging-derived sediment flux. "Difference 2" of "$J^{^{10}Be}_{riv}$ (insitu-DSS)" denotes the difference between $J^{^{10}Be}_{atm\text{-}lowl}$ and the $J^{^{10}Be}_{riv}$ using an in situ-derived sediment flux. The two grey dashed horizontal arrows correspond to the effective lowland riverine fluxes and show potential ^{10}Be radioactive decay during storage.

the large spatial scale of the Amazon basin, orographic effects causing the ^{10}Be flux to be a function of precipitation rate [e.g., *Graly et al.*, 2011] are averaged out. An estimate in the uncertainty in the geographic distribution of $F^{^{10}Be}_{met}$ is provided by the difference in ^{10}Be flux between modern and preindustrial deposition models [*Heikkilä and von Blanckenburg*, 2015] (see link to this data before the Acknowledgements). For the Amazon lowlands, the average flux and the difference, respectively, amount to approximately $1.4 \pm 0.1 \times 10^6$ at/cm^2/yr (Table 5). Similarly, *Willenbring and von Blanckenburg* [2010] noted that in the equatorial region, the Heikkilä ECHAM5 GCM model is ~20–50% higher in ^{10}Be flux relative to the GISS GCM used by *Field et al.* [2006]. These differences, however, do not explain the mismatch for all samples.

2. The missing atmospheric flux is deposited into an "inactive" area from which no sediment is exported and where all ^{10}Be radioactively decays with a half-life of 1.39 Myr. Therefore, this ^{10}Be is not contained in our sediment samples. What this means is that the total basin area A_{riv} in equation (1) might not represent the actual area from which the ^{10}Be flux is being delivered into the mainstream in the reactive or the dissolved form. We can employ equation (1) to derive the "active" (sediment and ^{10}Be delivering) area versus the inactive area by assuming that the deficit of $J^{^{10}Be}_{riv}$ relative to $J^{^{10}Be}_{atm}$ is proportional to the area not contributing ^{10}Be. We derive an inactive lowland area upstream of Óbidos of 1.6 to 2.6×10^6 km^2 (depending on whether the sedimentary flux $J^{^{10}Be}_{riv}$ was calculated using river gauging or in situ ^{10}Be, respectively, see Figure 6). When considering only the total lowland area of 4.14×10^6 km^2, the corresponding active lowland area ranges from 1.5 to 2.5×10^6 km^2. This is a much larger area than that of the active channel belt. Using a width of 35 km and a river length of 800 km for the Amazon at Óbidos (taken from *Wittmann and von Blanckenburg* [2009]), the channel belt area is 0.12×10^6 km^2. The estimate of the inactive area implies that between 38 and 64% of the Amazon lowland basin is not delivering ^{10}Be, in dissolved form or attached to sediment, into the mainstream.
3. A third possibility that differs from (2) assumes that all sediment from the lowland area is exported, but the missing ^{10}Be flux fraction has decayed radioactively in these lowland areas prior to export during sufficiently long storage. *Granger et al.* [2013] came to a similar conclusion for basins draining the coastal plains of the eastern United States. We use equation (3) to estimate this mean storage duration. We assume that only sediment stored in the lowland area (4.14×10^6 km^2) is affected by decay, such that $J^{^{10}Be}_{riv}$ in equation (3) is termed $J^{^{10}Be}_{riv\text{-}lowl}$. We use a lowland-specific $[^{10}Be]_{reac}$ of approximately 1×10^7 at/g (derived from the total basin-wide DSS-$[^{10}Be]_{reac}$ at Óbidos minus the average Andean DSS-$[^{10}Be]_{reac}$) as an approximated lowland nuclide concentration. For the same reason the depositional flux for the lowlands at Óbidos, $J^{^{10}Be}_{atm\text{-}lowl}$, is calculated according to equation (1). There, the same lowland A_{riv} (4.14×10^6 km^2) and a $F^{^{10}Be}_{met}$ of 1.4×10^6 at/cm$^2 \times$yr, characteristic for the lowland area, are used. The resulting $J^{^{10}Be}_{atm\text{-}lowl}$ at Óbidos is approximately 5.7×10^{22} at/yr (Figure 7). Two estimates for $J^{^{10}Be}_{riv\text{-}lowl}$ are 1.5×10^{22} at/yr and 1.05×10^{22} at/yr, using gauging- and in situ-derived sediment fluxes, respectively (equation (3)), where both estimates also include an estimate of the dissolved ^{10}Be flux (Table 5). We calculate the difference of the two $J^{^{10}Be}_{riv\text{-}lowl}$ estimates relative to $J^{^{10}Be}_{atm\text{-}lowl}$, called "difference 1" and "difference

2" in Figure 7. Difference 1 "$J_{riv}^{^{10}Be}$ (gauging-DSS)" (Figure 7) amounts to 4.2×10^{22} at/yr, and difference 2" $J_{riv}^{^{10}Be}$ (insitu-DSS)" amounts to 4.7×10^{22} at/yr. We estimate burial duration of circa 2.7 and 3.7 Myr (Figure 7). We note that these estimates are end-member (i.e., maximum) storage durations as they are based on the assumption that the entire lowland basin delivers sediment and ^{10}Be to the mainstream.

These end-member storage durations are not entirely different from the end-member burial durations detected in lowland sediment by in situ ^{26}Al/^{10}Be ratios measured in quartz in sandy bed load (see section 2.2) [*Wittmann et al*., 2011b]. However, such long periods were not detected in Andean-derived mainstream bed load sediment that dominates the mainstream bed load budget. From mixing calculations between this bed load end-member comprising coarser-grained floodplain sediment, and "fresh" Andean finer-grained bed load sediment, *Wittmann et al*. [2011b] estimated that a maximum of between 40% and 60% is presently admixed to nonburied fresh sediment in the central Amazon lowlands. It is, however, not clear whether these high fractions of admixing (derived from bed load samples) are also valid for meteoric cosmogenic nuclides measured from suspended sediment, given that both grain sizes are transported differently (i.e., channel bed load versus wash load also experiencing overbank deposition). Taking both systems into account, the most likely explanation for the flux deficit in meteoric ^{10}Be is a combination of possibilities (2) and (3), such that at the fringes of the inactive areas, where ^{10}Be has decayed, some sediment is reactivated and reaches the mainstream, whereas the largest fraction of the ^{10}Be deficit is generated in approximately 40% to 60% of areas that are fully inactive over long durations, and from which the sediment never reaches the mainstream.

5.2. Inferring Geomorphic Formation Regimes From ^{10}Be/^{9}Be in the Am-ox and X-ox Phases

Extracted am-ox and x-ox fractions of ^{10}Be, which together yield the total reactive ^{10}Be of the DSS data set, change in proportion from the Andes to the lowlands (section 4.2 and Figure 2). We observe an increase in DSS-derived $[^{10}Be]_{am\text{-}ox}$ relative to $[^{10}Be]_{x\text{-}ox}$ over this distance. Total suspended sediment $[^{9}Be]_{reac}$ in contrast experiences a minor decrease along the basin and no shift in proportions between amorphous and crystalline phases is observed (Figure 2B-1). The resulting increase in $(^{10}Be/^{9}Be)_{reac}$ from the Andes to the lowlands is thus mostly accommodated by $(^{10}Be/^{9}Be)_{am\text{-}ox}$. We attribute this increase to exchange processes with the dissolved phase. Amorphous to poorly crystalline Mn-Fe-(hydr-)oxides like, for example, ferrihydrite, exchange more readily with the dissolved phase than more crystalline materials due to their large reactive surface area [*Schwertmann et al*., 1999; *Waychunas et al*., 2005]. Thus, we infer that the increase in $(^{10}Be/^{9}Be)_{reac}$ from 2×10^{-10} to 5.4×10^{-10} for DSS samples from the Andes to the central lowlands reflects changes in $(^{10}Be/^{9}Be)_{am\text{-}ox}$ during floodplain storage. During storage, ^{10}Be delivered to floodplains is continuously adsorbed and/or incorporated into am-ox phases, such that this increase in ^{10}Be is a function of sediment residence time (section 5.3). Due to the continuous exchange between $^{10}Be_{am\text{-}ox}$ and $^{10}Be_{diss}$ as described by the solid-fluid partition coefficient K_d, $[^{10}Be]_{diss}$ increases simultaneously with $[^{10}Be]_{am\text{-}ox}$ along the river course (compare Tables 3 and 4).

The evolution of the x-ox phase is more complex, as it may evolve from amorphous precursor phases that age to crystalline solids [*Schwertmann et al*., 1999]. $(^{10}Be/^{9}Be)_{x\text{-}ox}$ thus likely reflect the composition of a dissolved phase at a time when the amorphous precursor phases formed. The transformation to stable crystalline Mn-Fe oxides that do not exchange with dissolved, floodplain-derived ^{10}Be, however, most likely occurred before entering the Amazon lowlands, as $(^{10}Be/^{9}Be)_{x\text{-}ox}$ are uniform from the Andes to the Amazon lowlands. We see evidence for such behavior in the comparison of dissolved ^{10}Be/^{9}Be with am-ox and x-ox-derived ^{10}Be/^{9}Be, respectively (Figure 5).

5.3. Increase in Meteoric-^{10}Be Concentrations in Lowland Basins During Sediment Transfer

We observe an increase in $[^{10}Be]_{reac}$ across the lowland basin (Figure 2B-2) by a factor of 2–3 in bed load (e.g. for the upper and lower Solimões reach, respectively, characterized by samples Pe 101 and Man 2.4) and by a factor of approximately 1.5 (approximately 1×10^{7} at/g, see section 5.1) in the DSS-$[^{10}Be]_{reac}$. Note that since this increase is observed for the Solimões reach where no sediment from cratonic shield is yet added, the increase in ^{10}Be concentration cannot be due to addition of shield sediment high in nuclide concentration. We can use the increase in $[^{10}Be]_{reac}$ across the floodplain as a direct measure of the sediment transfer time in a well-mixed active floodplain (see below), where the duration is so short that decay is negligible [*Lauer and Willenbring*, 2010; *Wittmann and von Blanckenburg*, 2009]. Such an increase of $[^{10}Be]_{reac}$ in the floodplain

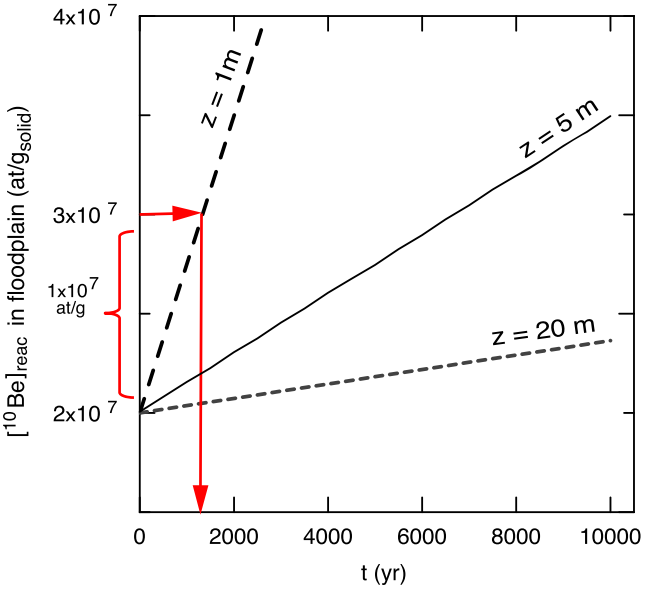

Figure 8. Model of ^{10}Be accumulation over time scales typical of active floodplain-channel interaction. Note that for these short time scales, decay of ^{10}Be is negligible. The observed increase in floodplain-derived $[^{10}Be]_{reac}$ (approximately 1×10^7 at/g) was added to an initial (Andean, depth-integrated DSS-derived) $[^{10}Be]_{reac}$ of approximately 2×10^7 at/g (Table 3). The predicted ^{10}Be inventory was calculated using equation (16) and converted into $[^{10}Be]_{reac}$ by assuming three different remobilization depths ($z = 1$, 5, 20 m; see text for details). For mean remobilization depths of approximately 1 m and 20 m, respectively, the observed increase in ^{10}Be across the floodplain would be produced during storage of circa 1.6 kyr and circa 29 kyr, respectively (the latter case is beyond the scale of the figure).

has not been predicted for meteoric ^{10}Be in the floodplain model of *Lauer and Willenbring* [2010]. We attribute this discrepancy to the small length scale of their local river model, whereas the model evaluating floodplain effects in a larger range of rivers by *Wittmann and von Blanckenburg* [2009] did not include an analysis of meteoric ^{10}Be.

Note that for in situ cosmogenic nuclides, an increase in ^{10}Be concentration across the lowlands is neither observed [*Wittmann et al.*, 2011a] nor predicted [*Lauer and Willenbring*, 2010; *Wittmann and von Blanckenburg*, 2009]. This is so for two reasons. (1) The production rates of in situ cosmogenic nuclides are lower in the lowlands than in the sediment-producing highlands. Thus, the relative increase in in situ concentration across the lowlands is lower. In contrast, meteoric ^{10}Be depositional fluxes are not altitude dependent below 3 km [*Willenbring and von Blanckenburg*, 2010]. (2) Meteoric ^{10}Be accumulation will mostly proceed in the upper, unburied part of a deposit that is rich in clay formed by overbank deposits. In contrast, the sandy fraction used for in situ nuclides might get shielded by these deposits, thus receiving reduced irradiation as shown by in situ ^{26}Al/^{10}Be-derived burial durations.

As noted above, a condition for the conversion of $[^{10}Be]_{reac}$ accumulation into a sediment transfer time is that we assume negligible burial in the active floodplain by ignoring that an unknown fraction of ^{10}Be may have decayed before being entrained in the active channel (scenario (3) in section 5.1). Thus, the increase in $[^{10}Be]_{reac}$ is attributed to the accumulation of ^{10}Be nuclides during surficial storage in the active part of the floodplain and hence represents a minimum storage time. This scenario is supported by the changes in the proportions of am-ox and x-ox phases (section 5.2).

Accordingly, we model the increase by a simple accumulation scenario where $[^{10}Be]_{reac}$ continuously accumulates in Amazon sediment during residence in the active floodplain (Figure 8). Using equation (6) in *Willenbring and von Blanckenburg* [2010], and assuming zero erosion of the stored lowland sediment, the sedimentary ^{10}Be inventory I (at/m^2), produced while the sediment is exposed to continuous atmospheric deposition $F_{met}^{^{10}Be}$, is given by

$$I_{10Be}(t) = \frac{F_{met}^{^{10}Be}}{\lambda}\left(1 - \exp^{-\lambda t}\right) + \left[^{10}Be\right]_{ini} \times \rho \times z \times \exp^{-\lambda t} \quad (16)$$

where t is in this case the sediment transfer time and the right-hand term in equation (16) reflects the decay-affected contribution of Andean-derived initial $[^{10}Be]_{reac}$ that is provided to the Amazon lowlands, ρ (kg/m^3) denotes the sediment density (2000 kg/m^3 for wet, silty sand [see *Balco et al.*, 2005]) and z (m) the remobilization depth of sediment. We use both ρ and z to convert the ^{10}Be inventory back into a ^{10}Be concentration. A lowland-specific $F_{met}^{^{10}Be}$ of 1.4×10^6 at/cm$^2 \times$ yr was used. An assumption of this parameterization is that all meteoric ^{10}Be added to the floodplain sediment is contained within this depth,

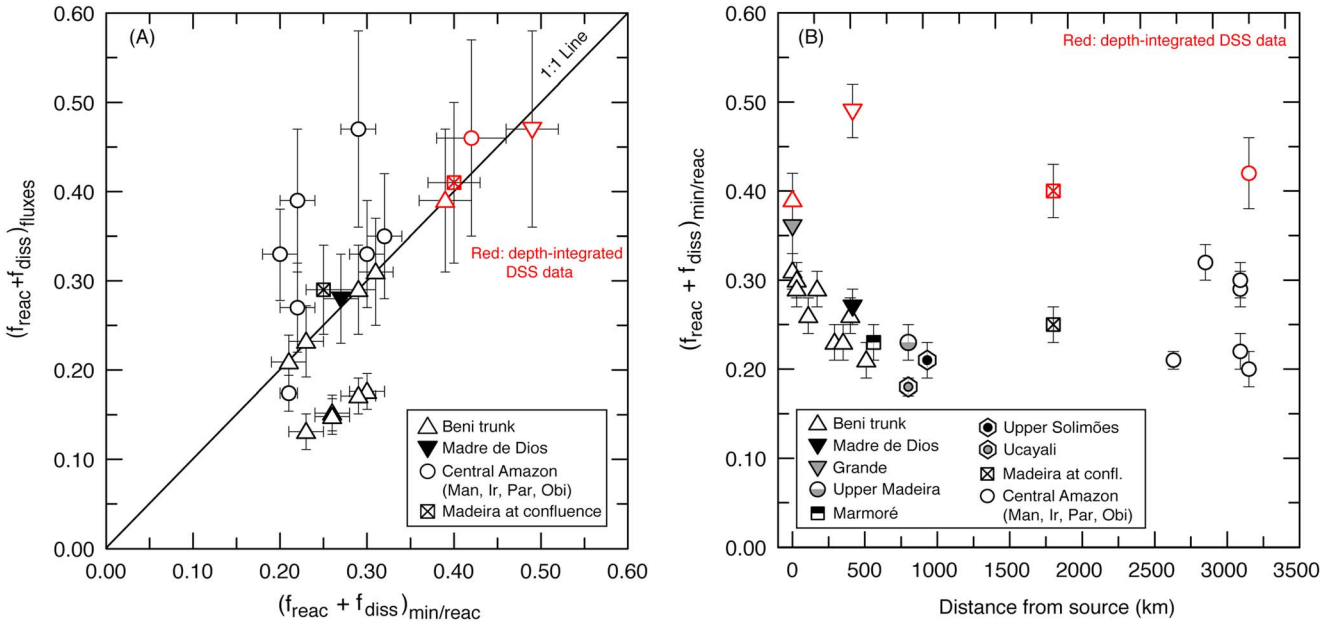

Figure 9. Fraction of ^{9}Be released during weathering, ($f_{reac}+f_{diss}$), in the Amazon basin. (a) $(f_{reac}+f_{diss})_{fluxes}$, derived according to equations (7a), (7b), and (8) using modern sediment load as sediment flux versus $(f_{reac}+f_{diss})_{min/reac}$ derived from equation (9). (b) $(f_{reac}+f_{diss})_{min/reac}$ versus distance from sediment source (in km). Note that all ($f_{reac}+f_{diss}$) values derived from bed load [^{9}Be] (black symbols) are most likely too low due to mineralogical differentiation by particle sorting. Uncertainties contain 1σ analytical uncertainties, and a 10% uncertainty on runoff and sediment flux, respectively. The Negro data are not shown.

such that the model is independent of ^{10}Be penetration depth [*Willenbring and von Blanckenburg*, 2010]. The initial $[^{10}Be]_{reac}$ is approximately 2×10^{7} at/g as determined from DSS samples measured on the Beni and Madre de Dios Rivers. For meteoric ^{10}Be that mostly binds to fine-grained clay particles, the main portion may be found in the topmost meter of floodplain sediment, as this layer is deposited during overbank spill. As a sensitivity analysis, we use equation (16) with $z=20$ m, for coarse, sandy bed load sediment mainly carrying in situ ^{10}Be at the bottom of the main channel [*Wittmann and von Blanckenburg*, 2009]. For the case of very shallow floodplain remobilization ($z=1$ m), characteristic for a topmost clay layer ladden with meteoric ^{10}Be that is deposited during overbank spill, a sediment transfer time in the floodplain of only circa 1.6 kyr is predicted to cause the additional accumulation of meteoric ^{10}Be across the floodplain. The deeper remobilization depth of 20 m requires a longer sediment transfer time of circa 29 kyr (not shown in Figure 8). Both predicted sediment transfer times are reasonable as other studies estimated similar residence times of sediment in the Amazon floodplain [*Dosseto et al*., 2006].

6. Weathering Intensities, Erosion Rates, and Denudation Rates

6.1. The Fraction of ^{9}Be Released During Weathering

The mobilized fraction of ^{9}Be, ($f_{reac}+f_{diss}$), quantifies Be release by primary mineral decomposition and is thus a proxy for weathering. We have calculated ($f_{reac}+f_{diss}$) from two independent means shown by equations (8) and (9). Here we compare $(f_{reac}+f_{diss})_{fluxes}$, estimated from the rivers' sedimentary and water fluxes, and $(f_{reac}+f_{diss})_{min/reac}$, based on measured $[^{9}Be]_{reac}$ and $[^{9}Be]_{min}$ in bed load or suspended river sediment. Both $(f_{reac}+f_{diss})_{fluxes}$ and $(f_{reac}+f_{diss})_{min/reac}$ from DSS samples (red symbols in Figure 9) are consistently higher than those from bed load using $[^{9}Be]_{reac}$ and $[^{9}Be]_{min}$ (black symbols in Figure 9 and Table 6). We attribute this observation to the fact that coarser grained bed load offers less surface area for scavenging of ^{9}Be. This grain size bias is best illustrated by the Negro, the only shield river where dissolved Be data are available. There, a $(f_{reac}+f_{diss})_{min/reac}$ of 0.222 ± 0.016 is calculated using bed load data (Table 6). However, when using the $[^{9}Be]_{reac}$ data from *Brown et al*. [1992], measured on surface suspended sediment, in combination with our $[^{9}Be]_{min}$, a $(f_{reac}+f_{diss})_{min/reac}$ of 0.83 ± 0.08 is calculated. This high value of ($f_{reac}+f_{diss}$) obtained from suspended sediment data is more consistent with weathering in the cratonic shield setting, as in these slowly eroding tectonically inactive regimes, most ^{9}Be is likely to have been removed from bedrock along with other

Table 6. ^{9}Be Weathering Degrees[a]

Sample	Calculated Using Mass Balance Approach[b]				$(f_{diss} + f_{reac})_{min/reac}$[c]
	^{9}Be f_{diss}	^{9}Be f_{reac}	^{9}Be f_{min}	$(f_{diss} + f_{reac})_{fluxes}$[d]	
Be 1 (average)	0.00039 ± 0.000039	0.310 ± 0.036	0.690 ± 0.084	0.310 ± 0.059	0.310 ± 0.024
Be-DSS[e]	0.00033 ± 0.000039	0.391 ± 0.044	0.608 ± 0.068	0.392 ± 0.082	0.392 ± 0.022
Be 2-1	0.00049 ± 0.000049	0.175 ± 0.020	0.82 ± 0.10	0.176 ± 0.025	0.298 ± 0.021
Be 2-2	0.00042 ± 0.000042	0.288 ± 0.034	0.711 ± 0.086	0.289 ± 0.053	0.289 ± 0.022
Be 3	0.00046 ± 0.000046	0.151 ± 0.017	0.85 ± 0.10	0.152 ± 0.020	0.263 ± 0.018
Be 4	0.00045 ± 0.000045	0.171 ± 0.019	0.83 ± 0.10	0.171 ± 0.024	0.292 ± 0.020
Be 8	0.00047 ± 0.000047	0.131 ± 0.015	0.87 ± 0.11	0.131 ± 0.016	0.231 ± 0.016
Be 10	0.00038 ± 0.000038	0.232 ± 0.027	0.77 ± 0.09	0.232 ± 0.038	0.232 ± 0.018
Be 12	0.0015 ± 0.00015	0.146 ± 0.016	0.85 ± 0.10	0.148 ± 0.019	0.255 ± 0.018
Md 15	0.0039 ± 0.00039	0.272 ± 0.032	0.724 ± 0.088	0.276 ± 0.050	0.273 ± 0.021
Md-DSS[e]	0.0039 ± 0.00039	0.492 ± 0.055	0.505 ± 0.056	0.47 ± 0.11	0.494 ± 0.032
OR 16					
Be 17	0.0019 ± 0.00019	0.207 ± 0.024	0.79 ± 0.10	0.209 ± 0.033	0.207 ± 0.016
Mar 18		0.231 ± 0.027	0.769 ± 0.093		0.231 ± 0.018
Mad 19					
Mad 20		0.226 ± 0.026	0.774 ± 0.094		0.226 ± 0.018
GR 19		0.365 ± 0.041	0.635 ± 0.071		0.365 ± 0.026
Pe 101		0.212 ± 0.025	0.79 ± 0.10		0.212 ± 0.017
Pe 107		0.0505 ± 0.0057	0.95 ± 0.12		0.177 ± 0.012
Man 2.4	0.024 ± 0.0031	0.150 ± 0.017	0.83 ± 0.10	0.174 ± 0.024	0.209 ± 0.015
Ir 1.75	0.052 ± 0.0052	0.297 ± 0.033	0.651 ± 0.079	0.349 ± 0.068	0.324 ± 0.023
Par 0.9	0.050 ± 0.0050	0.418 ± 0.049	0.532 ± 0.065	0.47 ± 0.11	0.288 ± 0.023
Par 1.2	0.069 ± 0.0069	0.201 ± 0.022	0.730 ± 0.089	0.270 ± 0.046	0.223 ± 0.016
Par 1.6	0.057 ± 0.0057	0.334 ± 0.039	0.609 ± 0.074	0.391 ± 0.083	0.224 ± 0.018
Par 2.2	0.062 ± 0.0063	0.272 ± 0.030	0.666 ± 0.081	0.334 ± 0.064	0.298 ± 0.021
Obi (average)	0.078 ± 0.0078	0.26 ± 0.03	0.675 ± 0.082	0.334 ± 0.065	0.310 ± 0.023
Obi-DSS[e]	0.051 ± 0.0078	0.40 ± 0.04	0.551 ± 0.062	0.45 ± 0.10	0.419 ± 0.036
Mad 0.3	0.0072 ± 0.00072	0.33 ± 0.04	0.667 ± 0.081	0.333 ± 0.066	0.328 ± 0.026
Mad 0.5	0.0077 ± 0.00077	0.175 ± 0.021	0.82 ± 0.10	0.183 ± 0.027	0.176 ± 0.014
Mad 1.8					
Mad-DSS[e]	0.010 ± 0.00074	0.40 ± 0.04	0.590 ± 0.066	0.410 ± 0.088	0.405 ± 0.028
Cb 2 (average)					0.380 ± 0.030
Cb 3					0.479 ± 0.039
Cb 5					0.213 ± 0.017
Cb 6					0.308 ± 0.024
Br 2					0.547 ± 0.039
Br 3					0.353 ± 0.025
Br 4					0.442 ± 0.031
Br 7 (average)					0.0896 ± 0.0064
Ne 0.6	0.90 ± 0.12	0.0225 ± 0.0025	0.0787 ± 0.0088	0.92 ± 0.32	0.222 ± 0.016
Region-averaged data from (if available) (1) Andean samples: Be 1-17, Md 15, Mar 18, Mad 19-20, Gr 19, Pe 101 and 107 (2) Amazon lowland samples: Man 2.4, Ir 1.75, Par 0.9-2.2, Obi, Mad 0.3-1.8					
Andes, DSS	0.00113 ± 0.000039	0.414 ± 0.049	0.585 ± 0.062	0.429 ± 0.092	0.443 ± 0.027
Lowlands, DSS	0.0359 ± 0.0043	0.399 ± 0.045	0.565 ± 0.064	0.44 ± 0.10	0.412 ± 0.032
Guyana Shield (Negro, using suspended sediment ^{10}Be data from *Brown et al.* [1992])					0.830 ± 0.080
Andes, Bed load	0.00084 ± 0.00010	0.201 ± 0.024	0.798 ± 0.095	0.202 ± 0.032	0.257 ± 0.019
Lowlands, Bed load	0.0377 ± 0.0042	0.276 ± 0.031	0.686 ± 0.084	0.314 ± 0.059	0.259 ± 0.019
Guyana Shield (Branco bed load data)					0.358 ± 0.025

[a] All *f*'s derived from bed load data may be biased due to grain size effects.
[b] Calculated using equations (7a), (7b), and (8) using modern sediment loads. Uncertainty includes analytical uncertanties, a 10% uncertainty on modern sediment flux, and a 10% uncertainty on water discharge. Note that for Cb and Br samples, lack of sediment load and discharge data prevented calculation of $(f_{reac} + f_{diss})_{fluxes}$.
[c] Calculated using equation (9); 1σ analytical uncertainties given.
[d] Note that where no ^{9}Be f_{diss} was measured, $(f_{reac} + f_{diss})_{fluxes}$ might be too low, especially for low-pH Shield Rivers.
[e] Calculated using depth-integrated $[^{9}Be]_{reac}$ and $[^{9}Be]_{min}$.

Table 7. K_d Values, Erosion, and Denudation Rate Data[a]

Sample	Corrected Linear K_d[b] (log mL/g)	E[^{10}Be]$_{full}$[c] (mm/yr)	E[^{10}Be][d] (mm/yr)	D_MET$_{fluxes}$[e] (mm/yr)	D_MET$_{min/reac-full}$[f] (mm/yr)	D_MET$_{min/reac}$[g] (mm/yr)	D_MET$_{min/reac-diss}$[h] (mm/yr)
Be 1 (average)	5.58	*1.07 ± 0.15*	*1.07 ± 0.10*	0.64 ± 0.22	0.64 ± 0.30	0.645 ± 0.094	0.25 ± 0.11
Be-DSS	5.58	0.445 ± 0.072	0.445 ± 0.044	0.60 ± 0.15	0.52 ± 0.24	0.526 ± 0.074	0.170 ± 0.075
Be 2-1	5.58	*1.30 ± 0.21*	*1.30 ± 0.16*	1.20 ± 0.24	0.70 ± 0.33	0.71 ± 0.11	
Be 2-2	5.58	*1.49 ± 0.23*	*1.49 ± 0.17*	0.80 ± 0.18			
Be 3	5.58	*1.41 ± 0.21*	*1.41 ± 0.15*	1.38 ± 0.25			
Be 4	5.58	*1.43 ± 0.21*	*1.43 ± 0.16*	1.43 ± 0.27			
Be 8	5.58	*1.91 ± 0.27*	*1.91 ± 0.19*	1.83 ± 0.31			
Be 10	5.58	*1.67 ± 0.24*	*1.67 ± 0.18*	1.00 ± 0.21	1.00 ± 0.47	1.00 ± 0.15	
Be 12	5.58	*1.55 ± 0.32*	*1.55 ± 0.28*	1.50 ± 0.35			
Md 15	4.90	*0.92 ± 0.11*	*0.925 ± 0.056*	0.53 ± 0.11	0.51 ± 0.37	0.535 ± 0.066	0.32 ± 0.13
Md-DSS	4.90	0.284 ± 0.039	0.284 ± 0.015	0.351 ± 0.085	0.29 ± 0.21	0.326 ± 0.035	0.174 ± 0.072
OR 16			*0.33 ± 0.10*				
Be 17	5.28	*1.35 ± 0.18*	*1.35 ± 0.12*	0.84 ± 0.16	0.84 ± 0.50	0.85 ± 0.12	
Mar 18			*0.88 ± 0.11*			0.474 ± 0.077	
Mad 19			*1.02 ± 0.12*				
Mad 20			*0.639 ± 0.072*			0.338 ± 0.052	
GR 19			*1.53 ± 0.34*			0.88 ± 0.21	
Pe 101			*0.498 ± 0.059*			0.232 ± 0.037	
Pe 107			*0.78 ± 0.12*				
Man 2.4[i]	5.58	*0.349 ± 0.050*	*0.349 ± 0.036*	0.195 ± 0.036			
Ir 1.75	5.58	*0.181 ± 0.026*	*0.181 ± 0.018*	0.091 ± 0.021			
Par 0.9	5.22	*0.201 ± 0.031*	*0.201 ± 0.023*	0.065 ± 0.018	0.101 ± 0.094	0.106 ± 0.017	0.127 ± 0.020
Par 1.2	5.22	*0.391 ± 0.058*	*0.391 ± 0.043*	0.155 ± 0.033			
Par 1.6	5.22	*0.523 ± 0.079*	*0.523 ± 0.059*	0.142 ± 0.036	0.24 ± 0.22	0.247 ± 0.039	0.163 ± 0.025
Par 2.2	5.22	*0.199 ± 0.030*	*0.199 ± 0.022*	0.094 ± 0.022			
Obi (average)	5.28	*0.361 ± 0.053*	*0.361 ± 0.039*	0.135 ± 0.059	0.15 ± 0.093	0.160 ± 0.024	0.137 ± 0.027
Obi-DSS	5.28	0.167 ± 0.029	0.167 ± 0.020	0.129 ± 0.035	0.140 ± 0.085	0.152 ± 0.023	0.108 ± 0.022
Mad 0.3	5.22	*0.295 ± 0.044*	*0.295 ± 0.032*	0.231 ± 0.055	0.23 ± 0.21	0.234 ± 0.036	0.192 ± 0.031
Mad 0.5	5.22	*0.67 ± 0.10*	*0.667 ± 0.077*	0.48 ± 0.10	0.48 ± 0.45	0.494 ± 0.077	0.358 ± 0.058
Mad 1.8	5.22	*0.100 ± 0.015*	*0.100 ± 0.011*				
Mad-DSS	5.22	0.218 ± 0.037	0.218 ± 0.025	0.249 ± 0.063	0.23 ± 0.21	0.240 ± 0.036	0.154 ± 0.036
Cb 2 (average)			*0.0508 ± 0.0065*			0.0209 ± 0.0035	
Cb 3			*0.0298 ± 0.0038*			0.0210 ± 0.0035	
Cb 5			*0.083 ± 0.016*			0.0333 ± 0.0075	
Cb 6			*0.0347 ± 0.0085*			0.0183 ± 0.0049	
Br 2			*0.162 ± 0.031*				
Br 3			*0.409 ± 0.078*			0.0328 ± 0.0070	
Br 4			*0.263 ± 0.049*				
Br 7 (average)			*0.286 ± 0.044*			0.173 ± 0.032	
Ne 0.6	3.80	*1.12 ± 0.15*	*1.12 ± 0.10*	0.028 ± 0.010	0.063 ± 0.064	0.115 ± 0.015	0.0520 ± 0.0088

[a] For DSS data, we used depth-integrated ^{9}Be and ^{10}Be concentrations for all calculations. All italic erosion rates from bed load samples might be biased due to grain size effects (see text). All uncertainties are "external" (including the uncertainty on $F_{10Bemet}$ given in Table 5).

[b] Corrected K_D values are derived using linear range of You et al.'s data set (see supporting information section S6), by manually reading the new values from the regression line at the corresponding average pH.

[c] Erosion rates calculated using equation (10) (including the q/K_d term). Uncertainty contains 1σ analytical uncertainties, the uncertainty on $F_{10Bemet}$, and a 10% uncertainty on Q. Where no E is given, K_d could not be estimated.

[d] Erosion rates calculated using equation (11) (ignoring the q/K_d term). Uncertainty contains 1σ analytical uncertainties as well as uncertainty on $F_{10Bemet}$.

[e] Denudation rates calculated using equation (12). Uncertainty contains 1σ analytical uncertainties, uncertainty on $F_{10Bemet}$, uncertainty on $(f_{reac} + f_{diss})_{fluxes}$ from Table 6, and a 4% uncertainty on $[^{9}Be]_{parent}$ ($2.5 \pm 0.1 \times 10^{-6}$ g/g). If ^{9}Be f_{diss} (Table 6) was not measured, then a D_MET$_{fluxes}$ was not calculated here.

[f] Denudation rates calculated according to full equation (13). Uncertainties contain 1σ analytical uncertainties as well as uncertainty on $F_{10Bemet}$ and a 4% uncertainty on $[^{9}Be]_{parent}$ ($2.5 \pm 0.1 \times 10^{-6}$ g/g). Where no D is given, $[^{9}Be]_{min}$ was not measured.

[g] Calculated according to simplified equation (15). Uncertainties contain 1σ analytical uncertainties as well as uncertainty on $F_{10Bemet}$, and a 4% uncertainty on $[^{9}Be]_{parent}$ ($2.5 \pm 0.1 \times 10^{-6}$ g/g). Where no D is given, $[^{9}Be]_{min}$ was not measured.

[h] Denudation rates from dissolved ^{10}Be/^{9}Be ratios are only given for samples where a $(^{10}Be/^{9}Be)_{diss}$ was directly measured. Uncertainties contain 1σ analytical uncertainties as well as uncertainty on $F_{10Bemet}$ and a 4% uncertainty on $[^{9}Be]_{parent}$ ($2.5 \pm 0.1 \times 10^{-6}$ g/g).

[i] For calculations we used a $[^{10}Be]_{diss}$ of 385 at/g_{water} that was taken from *Brown et al.* [1992].

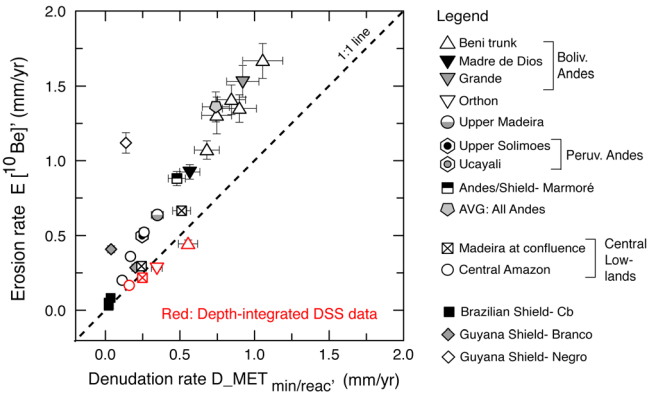

Figure 10. Simplified erosion rates $E_{[^{10}Be]'}$ (mm/yr), (equation (11)), versus simplified denudation rates $D\_MET_{min/reac}'$ (mm/yr) (equation (15)). Note that all erosion rates from bed load-derived $[^{10}Be]_{reac}$ are significantly higher than D's from $(^{10}Be/^{9}Be)_{reac}$, due to underestimates in $[^{10}Be]_{reac}$ from low specific surface area of large grains. Note that uncertainties are internal ones; i.e., the uncertainty given in Table 5 for $F_{met}^{^{10}Be}$ was not propagated here, as we compare within the same methodology.

cations during high degrees of weathering [*Johnsson et al.*, 1991]. Therefore, we conclude that estimates of $(f_{reac}+f_{diss})$ based on bed load data are too low and are unlikely to represent a reliable weathering proxy in settings where the majority of sediment flux is derived from suspended sediment transport. Our subsequent analyses rely on depth-integrated data to calculate $(f_{reac}+f_{diss})$ (Table 6).

For the Beni and Madre de Dios, DSS-derived $(f_{reac}+f_{diss})_{min/reac}$ is 0.44 ± 0.03, and very similar values of 0.43 ± 0.10 are derived from $(f_{reac}+f_{diss})_{fluxes}$. For samples Obi and Mad in the lowlands, DSS-derived $(f_{reac}+f_{diss})_{min/reac}$ is 0.41 ± 0.03, and a similar value of 0.43 ± 0.10 for $(f_{reac}+f_{diss})_{fluxes}$ is derived. Thus, the $(f_{reac}+f_{diss})$ does not differ between the Andes and the lowlands when using depth-integrated suspended sediment samples for calculation of $(f_{reac}+f_{diss})$.

This observation is, to a first order, consistent with invariant $[^{9}Be]_{reac}$ in the basin from the Andes to the lowlands (Figures 2A.1 and 2B.1). Further, this observation is consistent with the distribution of extracted am-ox and x-ox phases that combine to reactive ^{9}Be (Table 3 and section 4.2). Both leached phases are contributing similar fractions to total $[^{9}Be]_{reac}$ within Andean and lowland suspended sediment samples, indicating no change in $[^{9}Be]_{reac}$ along the transport from the Andes to the lowlands. Our results thus indicate that ^{9}Be is mainly weathered from bedrock in the source area and that $(f_{reac}+f_{diss})$ does not depend on the prevailing D. Along the lowland reach from the Andean foothills to the central lowlands, deposited sediments are already preweathered and potentially depleted of their ^{9}Be. This conclusion is in line with *Bouchez et al.* [2012, 2014] who found only minor increases in weathering during transfer of sediment through the floodplains.

A model for using $^{10}Be/^{9}Be$ dissolved in seawater and in authigenic marine sediment (reflecting paleoseawater) has been developed to quantify sedimentary and dissolved trace metal input into the oceans [*von Blanckenburg and Bouchez*, 2014]. The independence of $(f_{reac}+f_{diss})$ on the prevailing D fulfills the requirement for paleoseawater $^{10}Be/^{9}Be$ to reflect paleo-D over Myr time scales [*von Blanckenburg and Bouchez*, 2014].

6.2. Comparing Erosion Rates From $[^{10}Be]_{reac}$ With Denudation Rates From $^{10}Be/^{9}Be$ Ratios

Meteoric denudation rates corrected for retentivity issues ($D\_MET_{min/reac\text{-}full}$, equation (13)) versus simplified meteoric denudation rates ($D\_MET_{min/reac}'$, equation (15)) agree well for all geomorphic regions of the Amazon basin, except for the Negro, where ignoring retentivity leads to a bias in D of approximately 50% (Table 7 and supporting information section S6). These $D\_MET_{min/reac\text{-}full}$ and $D\_MET_{min/reac}'$, respectively, are based on the $[^{9}Be]_{min}/[^{9}Be]_{reac}$ ratio (equations (13) and (15)). This means that the resulting denudation rates might be biased by grain size effects. However, comparison with D_MET_{fluxes} (Table 7), calculated according to equation (12) without the $[^{9}Be]_{min}/[^{9}Be]_{reac}$ ratio, shows excellent agreement, except for D derived for the Negro, where D_MET_{fluxes} are approximately 50% lower than $D\_MET_{min/reac\text{-}full}$.

Erosion rates $E_{[^{10}Be]_{full}}$, fully corrected for retentivity, versus simplified erosion rates $E_{[^{10}Be]'}$ (equations (10) and (11) and Table 7) agree well but are systematically *higher* than denudation rates $D\_MET_{min/reac}'$ (equation (15)) when using bed load data. However, when using depth-integrated DSS data (Figure 10), the two fluxes agree. Note that when using *Brown et al.* [1992] data set on surface suspended sediment in the Orinoco (supporting information section S7), a similar agreement between E and D is observed. However, an erosion rate E cannot be higher than a denudation rate D. Hence, an obvious bias of E from bed load samples exists that is due to grain size effects resulting in an overestimation of E as $[^{10}Be]_{reac}$ are too low in coarse-grained sediment.

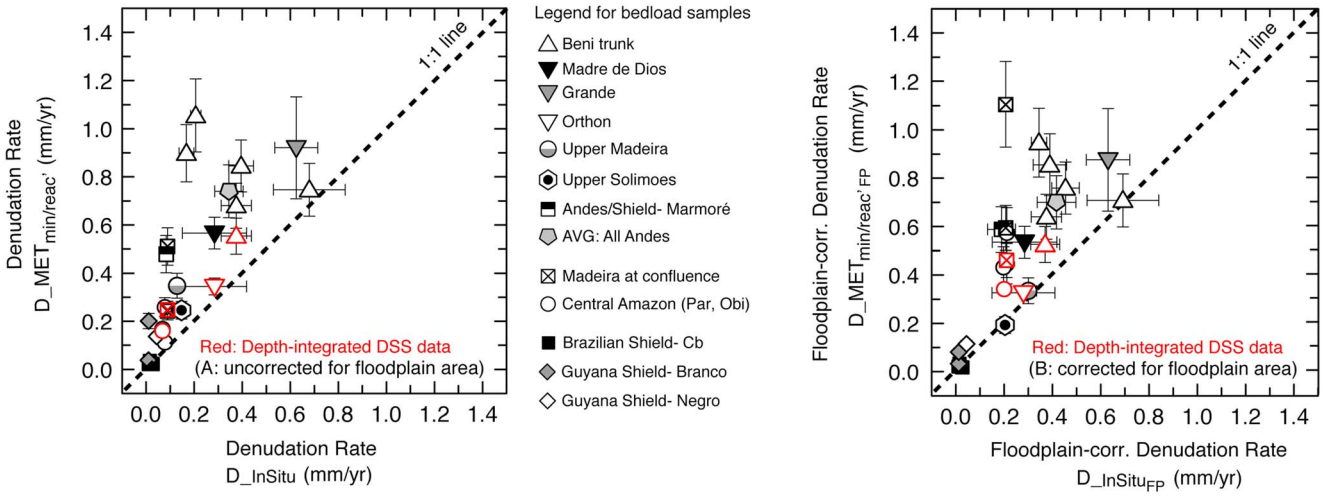

Figure 11. (a) Simplified denudation rates D_MET$_{min/reac}$' (mm/yr) (equation (15)) versus denudation rates D_insitu from in situ-^{10}Be (*Wittmann et al.* [2009, 2011a]; Table 1b), all uncorrected for floodplain area effect. (b) Floodplain-corrected denudation rates D_MET$_{min/reac'FP}$ (mm/yr) (from equation (15) but using a (^{10}Be/^{9}Be)$_{reac}$ of 2.3×10^{-10} for all lowland rivers, and the source area-specific $F^{^{10}Be}_{met}$ (Table 5)), plotted versus denudation rates D_insitu$_{FP}$, corrected for floodplain area ([*Wittmann et al.*, 2009, 2011a]; Table 1b). Uncertainties contain 1σ analytical uncertainties on [^{10}Be]$_{reac}$ and [^{9}Be]$_{reac}$, a 4% uncertainty on [^{9}Be]$_{parent}$ (Table 7), and we included here the uncertainty given in Table 5 for $F^{^{10}Be}_{met}$, such that uncertainties are external ones that should be used when comparing different methods. For D_insitu and D_insitu$_{FP}$, we used the uncertainties given in Table 1b.

This explanation, however, does not serve to clarify why erosion rates from DSS samples are close to DSS-derived denudation rates (red symbols in Figure 10). Only in kinetically limited settings, where mineral dissolution is negligible as erosion is rapid [*West et al.*, 2005], should D equal E. For DSS samples that are considered to be representative of Amazon sediment transport in terms of [^{10}Be]$_{reac}$, the following methodological (option 1), geological (2), and combined (3) explanations are offered for $D \approx E$:

1. Both D_MET$_{min/reac}$' and D_MET$_{fluxes}$ can be underestimated if ($f_{reac} + f_{diss}$) is overestimated. Such bias can be introduced by grain size-dependent sorting as both $(f_{reac} + f_{diss})_{min/reac}$ and $(f_{reac} + f_{diss})_{fluxes}$ make use of [^{9}Be]$_{reac}$ (equations (8) and (9)). However, in coarse bed load samples, in which [^{9}Be]$_{reac}$ is most likely underestimated, $(f_{reac} + f_{diss})_{fluxes}$ and $(f_{reac} + f_{diss})_{min/reac}$ are lowest (Figure 9). Still D is lowest relative to E in bed load samples (Figure 10). Hence, we regard this explanation as unlikely.
2. Weathering rates might be negligible compared to total denudation. Evidence for this explanation is reported in *Bouchez et al.* [2014], who find (a) an overall low degree of weathering in rivers draining Andean sediments, an observation that these authors attribute to the fact that Andean source rocks are recycled, preweathered metasedimentary rocks, and (b) that the dissolved weathering export only increases slightly across the lowlands [*Bouchez et al.*, 2014].
3. Estimates of D will be too low if a value for [^{9}Be]$_{parent}$ is used that exceeds the true value. We assume a [^{9}Be]$_{parent}$ of 2.5×10^{-6} g/g for all three geomorphic parts of the Amazon basin throughout. Given the large size of the basin it is unlikely that [^{9}Be]$_{parent}$ values differ much from this global value inferred for felsic igneous and sedimentary rocks [*von Blanckenburg et al.*, 2012]. One exotic explanation is offered in the upper Brazilian Shield, where the ^{9}Be is partly portioned into emerald (a form of beryl) deposits. If this Be silicate resists weathering and is instead enriched in placer deposits [*Barton and Young*, 2002], then the remaining weatherable silicates contain much lower [^{9}Be]$_{parent}$.

We are unable to definitely exclude any of these explanations. However, we regard both D and E determined from DSS samples to be most reliable due to their presumably representative [Be]$_{reac}$. If so, the agreement between D and E confirms the low degree of weathering and the low weathering rates in the lowlands of the Amazon basin (section 6.1). We proceed with a comparison to in situ-derived denudation rates, which provide an independent estimate of D in the Amazon basin.

6.3. Comparison of Meteoric-Derived With In Situ-Derived Denudation Rates

We can compare our D_MET$_{min/reac}$' to two denudation rate estimates available from in situ ^{10}Be [*Wittmann et al.*, 2009, 2011a]. The first estimate differs from the second by application of the floodplain correction.

Floodplain-uncorrected denudation rates comprise basin-wide rates (D_insitu), and floodplain-corrected denudation rates integrate over the sediment source area only (D_insitu_{FP}) (see section 2.2 for a detailed explanation). In order to compare both methods, we evaluate either floodplain-corrected or floodplain-uncorrected *D* in Figure 11.

A floodplain correction of $D\_MET_{min/reac}'$, resulting in $D\_MET_{min/reac'FP}$, was carried out for lowland samples based on equation (15), but using a $F_{met}^{^{10}Be}$ of each sample's specific sediment source area only (Table 5) and using an average $(^{10}Be/^{9}Be)_{reac}$ of 2.3×10^{-10}. This average floodplain-corrected ratio was derived by averaging the depth-integrated $[^{10}Be]_{reac}$ of the Andean Beni and Madre de Dios samples divided by the respective averaged depth-integrated $[^{9}Be]_{reac}$ of the same samples. The mean floodplain-uncorrected $D\_MET_{min/reac'}$ is 0.25 mm/yr (average from all bed load samples at Par, Obi, and Man; Table 7), and the mean floodplain-corrected $D\_MET_{min/reac'FP}$ for the same sample suit is 0.63 mm/yr, respectively. For DSS-samples, the mean floodplain-uncorrected $D\_MET_{min/reac'}$ of the Madeira and Óbidos profiles is 0.20 mm/yr, whereas the mean floodplain-corrected $D\_MET_{min/reac'FP}$ for Mad-DSS and Obi-DSS is 0.40 mm/yr. Considering the entire data set, we find that with a few exceptions, rates agree within a factor of 2 (Figure 11), and DSS-derived meteoric denudation rates agree even better, showing that these samples most likely best represent the overall erosion.

As initial explanations for $D\_MET_{min/reac}'$ exceeding D_insitu, we offer those that have been already explored in section 5.1 to explain the deficit in exported $^{10}Be_{met}$ flux: an overestimate of $F_{met}^{^{10}Be}$ or a deficit in ^{10}Be from radioactive decay during storage. However, the differences in denudation rate between the two methods might also be real. They can result from the following:

1. Potentially different integration times between the two methods. The integration time calculated from in situ ^{10}Be is a function of the denudation rate itself, i.e., the time required to erode a layer of thickness z^*, where z^* is the adsorption depth scale for in situ cosmogenic nuclides that is 60 cm in rocks or approximately 100 cm in soils [*von Blanckenburg*, 2005]. For meteoric ^{10}Be, the adsorption coefficient k, 1/cm, describing the decrease of meteoric nuclide concentration with depth [*Willenbring and von Blanckenburg*, 2010] is unknown, and ^{10}Be penetration depth varies strongly in soil [*Graly et al*., 2010]. However, we can assume that the meteoric ^{10}Be penetration depth corresponds to the thickness of Andean soils, which are relatively thin (the mean Andean soil depth is most likely thinner than 100–200 cm [*Haase*, 1992]), owing to fast erosion. In shale rocks that are widely distributed in the Andes, for example, meteoric ^{10}Be penetrates only approximately 1 m [*West et al*., 2013]. Dividing the soil depth by an Andean denudation rate of approximately 0.4 mm/yr [*Wittmann et al*., 2009, 2011a], we calculate an integration time scale of 2.5 to 5 kyr for both methods. Thus, using this crude approach, the integration times for both methods are very similar, and we exclude them as a cause for the discrepancy. *Foster et al*. [2015] recently demonstrated similar integration time scales for both methods for an intensively investigated watershed in Colorado. Note, however, that this explanation most likely is only valid in Andean settings, whereas in lowland soils, k is completely unknown and meteoric ^{10}Be could potentially penetrate much deeper.
2. A lithologic control on *D*. The control of lithology on *D* might be exerted by two interlinked processes: (1) erodibility of the bedrock and (2) preferential fluvial transport. Regarding the first possibility, grain sizes sampled for meteoric denudation rates might be mainly derived from more rapidly eroding shale-rich lithologies, whereas quartz-rich bedrock types (e.g., granitoid) supply sand-sized quartz at lower denudation rates, due to their overall lower erodibility [*Kühni and Pfiffner*, 2001]. Second, these different lithologies might exhibit different modes of transport in large rivers. Based on Li isotope data, *Dellinger et al*. [2014] suggested that lithologies generating fine-grained sediments (e.g., shales) are overrepresented in suspended sediments, whereas grains derived from igneous rocks are mainly incorporated into coarse sediments (e.g., bed load). Indeed, fine-grained clastic sedimentary lithologies cover a substantial fraction of the Amazon basin [*Gaillardet et al*., 1999; *Dellinger et al*., 2014]. Hence, if this lithological bias exists, it may actually result in differing denudation rates for the two methods.

7. Conclusions

The new erosion and weathering proxy making use of ratios of meteoric ^{10}Be to stable ^{9}Be provides denudation rates and weathering intensities that are in good agreement with independent measures of Earth surface change. The most important findings are the following:

1. $^{10}Be/^{9}Be$ ratios agree within a factor of 2 between dissolved Be (diss), measured from river water, and reactive (reac) values, comprising summed amorphous and crystalline Mn-Fe-(hydr-)oxides extracted chemically from both bed load and suspended sediment. Both reactive and dissolved Be hence reflect the catchments' denudation rate.
2. Where the crystalline and the amorphous oxide phases were separately analyzed for Be, $^{10}Be/^{9}Be$ in the dissolved phase ($(^{10}Be/^{9}Be)_{diss}$) agrees better with $^{10}Be/^{9}Be$ in the amorphous phase ($(^{10}Be/^{9}Be)_{am\text{-}ox}$), showing continuous exchange in the main stem of the Amazon River. In contrast, $^{10}Be/^{9}Be$ in crystalline oxides displays a memory from the weathering zone in the source area. Different oxide fractions therefore disclose the weathering processes in the mountains versus the exchange processes in the floodplain.
3. The $[^{10}Be]_{reac}$ in bed load samples is too low compared to expected erosion rates, due to the coarse grain size of the bed load samples. This bias can be circumvented by using a correlation that we found between $[^{10}Be]_{reac}$ and the Al/Si ratios in suspended sediment depth profiles. We use this correlation with representative estimates of Al/Si to calculate depth-integrated $[^{10}Be]_{reac}$ and $[^{9}Be]_{reac}$. These concentrations we regard as representative of the bulk of the sedimentary Be flux. This approach can now be used to resolve the grain size problem impairing the use of $[^{10}Be]_{reac}$ to measure erosion rates in fine-grained river sediment.
4. We find an increase in $[^{10}Be]_{reac}$ from the Andes to the lowlands, but no increase in $[^{9}Be]_{reac}$ over the same distance. The increase in $[^{10}Be]_{reac}$ we attribute to continuous meteoric deposition of ^{10}Be within the floodplain. From modeling ^{10}Be inventories, the observed increase in ^{10}Be would be facilitated by a minimum sediment transfer time of 1.6 to 29 kyr, excluding ^{10}Be decay during burial.
5. We note that this increase in $[^{10}Be]_{reac}$ (and correspondingly $(^{10}Be/^{9}Be)_{reac}$) from the Andes to the lowlands is a feature not observed for published in situ ^{10}Be concentrations that are uniform across the same distance as measured on fine-grained sandy bed load. One difference between the two methods is atmospheric scaling that is, for in situ-nuclide production, reduced significantly from mountainous to low-elevation floodplain areas. The meteoric ^{10}Be flux, however, does not differ much across altitude; therefore, the source-area derived meteoric signal is more readily increased by meteoric depositional flux during surficial floodplain transfer.
6. A steady state ^{10}Be flux balance is not necessarily fulfilled in the Amazon basin: at the outlet of the basin, the exported ^{10}Be flux derived from suspended sediment or in situ ^{10}Be-derived sedimentary load concentrations is approximately 15–80% lower than the depositional flux. This mismatch may simply be due to overestimating the Holocene-averaged atmospheric ^{10}Be flux, estimated here from the atmospheric cosmogenic nuclide production functions combined with a global circulation model [*Heikkilä et al*., 2013a, 2013b]. However, other geological explanations for the flux deficit can be invoked that account for sediment transport and deposition processes typical for large lowland basins. For example, not all ^{10}Be deposited over the basin may be delivered into the mainstream. Using the deficit we infer that an area comprising 40 to 60% of the basin is inactive, meaning that this area does not exchange its sediment with the main channel. A second possibility is that even if all sediment exchanges with the main channel, some of it may have been stored previously for approximately 3 to 4 Myr during which meteoric ^{10}Be has decayed.

Our primary findings regarding weathering, erosion, and denudation rates determined from the *von Blanckenburg et al*. [2012] framework are summarized below. Bearing in mind that the steady state assumption for meteoric ^{10}Be flux might not be satisfied, our analysis emphasizes comparison of calculated erosion rates E (using meteoric $[^{10}Be]_{reac}$) and denudation rates D (from $(^{10}Be/^{9}Be)_{reac}$ and $(^{10}Be/^{9}Be)_{diss}$) with published in situ values. Using a ^{9}Be mass balance, we can explore relative degrees of weathering from flux fractions of reactive and dissolved ^{9}Be released during weathering.

7. The mobile fraction of ^{9}Be released during weathering of rock to soil amounts to roughly 40%. This value is invariant from the Andes across the lowlands to the mouth of the Amazon, indicating the absence of weathering of Be-containing minerals in the Amazon floodplain over the timescale and within the uncertainty of the method.
8. Erosion rates from $[^{10}Be]_{reac}$ are overestimated from bed load samples, but when using depth-integrated suspended sediment $[^{10}Be]_{reac}$, erosion rates agree with denudation rates from $(^{10}Be/^{9}Be)_{reac}$. The published contribution of weathering to total denudation in the Amazon basin is low at $<$20% (explained by the prevalence of clastic sedimentary lithologies), such that E may indeed roughly equal D in the Amazon basin.
9. Denudation rates from meteoric $^{10}Be/^{9}Be$ ratios measured from bed load, suspended sediment, and water samples from Amazon rivers are systematically higher but agree within a factor of approximately 2 or better, with published values of D from in situ cosmogenic nuclides in quartz. This overall agreement shows that by using the $(^{10}Be/^{9}Be)_{reac}$ ratio, grain size bias introduced by particle sorting is removed.

10. Denudation rates from $(^{10}Be/^{9}Be)_{reac}$ slightly exceed those from ^{10}Be produced in situ in river quartz. The only possible methodological explanation is an overestimate in atmospheric flux, as all other methods-related possibilities ($^{9}Be_{parent} > 2.5 \times 10^{-6}$ g/g, underestimation of $(f_{reac} + f_{diss})$ due to particle sorting) would further increase the difference. However, as we have no unambiguous evidence for an overestimate in the atmospheric flux, we favor a geological explanation: by sampling fine-grained material for meteoric ^{10}Be, possibly more rapidly eroding lithologies such as shales are integrated. Sand-sized quartz in contrast may average over more resistant granitoid lithologies, leading to lower values of *D*.

The overall consistency within a factor of 2 or better between meteoric and published in situ denudation rates is encouraging for further work. The much smaller sample amounts required, the weathering information carried by the ^{9}Be-bearing fractions, and the applicability to a large range of lithologies, grain sizes, and sedimentary records extends the range of potential application settings considerably over those presently provided by in situ-derived denudation rates measured in quartz.

Notation

$F^{^{10}Be}_{met}$	at/m^2/yr	Average depositional flux of meteoric ^{10}Be into a given basin (as read from distribution maps and corrected for variations caused by changes in magnetic field strength)
$[^{9}Be]_{parent}$ $[^{9}Be]_{diss}$ $[^{9}Be]_{reac}$ $[^{9}Be]_{min}$	g/kg g/L g/kg g/kg	Concentration of ^{9}Be in parent bedrock (parent), assumed to be close to 2.5×10^{-6} g/g in average felsic rock or clastic sediment; this initial Be concentration is partly released into river water (diss), adsorbed or precipitated onto river sediment (reac), or remains after primary mineral dissolution (min)
$[^{10}Be]_{diss}$ $[^{10}Be]_{reac}$ $[^{10}Be]_{min}$	at/L at/kg at/kg	Concentration of meteoric ^{10}Be in the respective phases (see above)
$(^{10}Be/^{9}Be)_{reac}$ $(^{10}Be/^{9}Be)_{diss}$		^{10}Be(meteoric)/^{9}Be ratio in reactive and dissolved fractions (see above)
$A_{riv,i}$	m^2	Area of a given subbasin (i) that contributes ^{10}Be
$J^{^{9,10}Be}_{riv}$ $J^{^{9,10}Be}_{riv\_reac}$ $J^{^{9,10}Be}_{riv\_diss}$ $J^{^{9}Be}_{riv\_min}$	at/yr (^{10}Be) g/yr (^{9}Be)	Total (riv) meteoric flux of ^{10}Be and stable ^{9}Be exported by the river system that is the sum of riverine solid reactive (adsorbed and secondary solids, termed reac) and dissolved (diss) fractions calculated based on the rivers' sedimentary and water fluxes and their respective basin areas. ^{9}Be can also be transported in the residual primary mineral phase (min). Note that meteoric ^{10}Be is not contained in primary minerals, and in situ ^{10}Be contained in primary minerals is negligible in its concentration
$J^{^{10}Be}_{riv-lowl}$	at/yr	The portion of the exported ^{10}Be flux that was added to sediment by exposure to atmospheric ^{10}Be flux in the lowlands
$J^{^{10}Be}_{atm}$	at/yr	Basin-wide atmospheric ^{10}Be flux, which is the depositional flux $\left(F^{^{10}Be}_{met}\right)$ over a given surface area A_{riv}
K_d	L/kg	Solid/fluid partition coefficient that links Be concentrations in the reactive and dissolved phases
$\left(f^{^{9}Be}_{reac} + f^{^{9}Be}_{diss}\right)_{fluxes}$ $\left(f^{^{9}Be}_{reac} + f^{^{9}Be}_{diss}\right)_{min/reac}$		Mobile flux fraction of ^{9}Be released from primary minerals during weathering that is partitioned into the reactive (reac) and dissolved (diss) phase, calculated based on the rivers' sedimentary and dissolved fluxes (fluxes), or calculated using measured $[^{9}Be]_{reac}$ and $[^{9}Be]_{min}$ (min/reac)
^{9}Be-f_{reac} ^{9}Be-f_{diss} ^{9}Be-f_{min}		Nondimensional fractional fluxes of ^{9}Be, i.e., ^{9}Be-f_{reac} + ^{9}Be-f_{diss} + ^{9}Be-f_{min} = 1
Q_i	L/yr	Water discharge
q	m^3/m^2/yr or m/yr	Runoff (area-normalized water flux)

E_i	kg/m^2/yr	Erosion rate for a given subbasin, derived independently from modern suspended sediment measurements or from in situ-derived cosmogenic ^{10}Be
$E_{[10Be]full}$ $E_{[10Be]'}$	kg/m^2/yr	Erosion rate calculated from [^{10}Be]$_{reac}$, including the q/K_d correction for loss of ^{10}Be into the dissolved phase (full); and simplified by omitting the q/K_d correction for dissolved loss (')
D_MET$_{fluxes}$	kg/m^2/yr	Denudation rate; calculation based on the (^{10}Be/^{9}Be)$_{reac/diss}$ and $\left(f^{^9Be}_{reac} + f^{^9Be}_{diss}\right)_{fluxes}$
D_MET$_{min/reac\ -\ full}$ D_MET$_{min/reac}$'	kg/m^2/yr	Denudation rate based on the (^{10}Be/^{9}Be)$_{reac/diss}$ and $\left(f^{^9Be}_{reac} + f^{^9Be}_{diss}\right)_{min/reac}$ including the q/K_d correction for dissolved loss (full) and simplified by omitting the q/K_d correction for dissolved loss (')
D_insitu D_insitu$_{FP}$	kg/m^2/yr	Denudation rate from in situ-^{10}Be nuclide concentrations in quartz, where the subscript "FP" indicates the application of a floodplain correction. Conversion of erosion and denudation rates from units of kg/m^2/yr to m/yr is done by using a bedrock density of 2600 kg/m^3
W	kg/m^2/yr	Weathering rate, meaning surface lowering by rock dissolution and transport in the river dissolved phase
I_{10Be}	at/m^2	Inventory of ^{10}Be, meaning the amount of ^{10}Be contained in a vertical column of soil or sediment over a given area

Acknowledgments

We thank CLIM-AMAZON for partial financial support. Most samples were collected within the framework of the HyBAm project, a collaboration of the French IRD with South American Institutes and Universities. We sincerely thank U. Heikkilä for discussions on depositional flux and GCM models and H. Haedke for help preparing flux maps and providing an in situ denudation rate for the Orinoco. A. Süssenberger is thanked for processing some suspended sediment depth samples, H. Rothe and H. Schopka for HR-MC-ICP-MS support, C. Schulz for lab support, R. Naumann for XRD analyses, J. Schuessler for OES support, and S. Heinze and S. Binnie from Cologne University for AMS support. We also thank A. Laraque for providing an Orinoco River sample. D. Granger, K. Ferrier, and Editor J. Buffington are sincerely thanked for constructive reviews. Supporting data are included as supporting information in a SI file; any additional data may be obtained from H. Wittmann (e-mail: wittmann@gfz-potsdam.de). Supporting data on the Holocene depositional ^{10}Be flux maps can be accessed at http://dx.doi.org/10.5880/GFZ.3.4.2015.001.

References

Aldahan, A., H. P. Ye, and G. Possnert (1999), Distribution of beryllium between solution and minerals (biotite and albite) under atmospheric conditions and variable pH, *Chem. Geol.*, *156*(1–4), 209–229.

Allard, T., M. Ponthieu, T. Weber, N. Filizola, J. L. Guyot, and M. Benedetti (2002), Nature and properties of suspended solids in the Amazon Basin, *Bull. Soc. Geol. Fr.*, *173*(1), 67–75.

Barton, M. D., and S. Young (2002), Non-pegmatitic deposits of beryllium: Mineralogy, geology, phase equilibria and origin, *Rev. Mineral. Geochem.*, *50*(1), 591–691, doi:10.2138/rmg.2202.50.01.

Balco, G., J. O. H. Stone, and C. Jennings (2005), Dating Plio-Pleistocene glacial sediments using the cosmic-ray-produced radionuclides 10Be and 26Al, *Am. J. Sci.*, *305*(1), 1–41, doi:10.2475/ajs.305.1.1.

Bouchez, J., F. Métivier, M. Lupker, L. Maurice, M. Perez, J. Gaillardet, and C. France-Lanord (2010), Prediction of depth-integrated fluxes of suspended sediment in the Amazon River: Particle aggregation as a complicating factor, *Hydrol. Processes*, *25*(5), 778–794, doi:10.1002/hyp.7868.

Bouchez, J., J. Gaillardet, C. France-Lanord, L. Maurice, and P. Dutra-Maia (2011a), Grain size control of river suspended sediment geochemistry: Clues from Amazon River depth profiles, *Geochem. Geophys. Geosyst.*, *12*, Q03008, doi:10.1029/2010GC003380.

Bouchez, J., M. Lupker, J. Gaillardet, C. France-Lanord, and L. Maurice (2011b), How important is it to integrate riverine suspended sediment chemical composition with depth? Clues from Amazon River depth-profiles, *Geochim. Cosmochim. Acta*, *75*(22), 6955–6970, doi:10.1016/j.gca.2011.08.038.

Bouchez, J., J. Gaillardet, M. Lupker, P. Louvat, C. France-Lanord, L. Maurice, E. Armijos, and J.-S. Moquet (2012), Floodplains of large rivers: Weathering reactors or simple silos?, *Chem. Geol.*, *332-333*, 166–184, doi:10.1016/j.chemgeo.2012.09.032.

Bouchez, J., J. Gaillardet, and F. von Blanckenburg (2014), Weathering intensity in Lowland River Basins: From the Andes to the Amazon mouth, *Procedia Earth Planet. Sci.*, *10*, 280–286, doi:10.1016/j.proeps.2014.08.063.

Bourlès, D., G. M. Raisbeck, and F. Yiou (1989), ^{10}Be and ^{9}Be in marine sediments and their potential for dating, *Geochim. Cosmochim. Acta*, *53*(2), 443–452.

Brown, E. T., J. M. Edmond, G. M. Raisbeck, D. Bourlès, F. Yiou, and C. I. Measures (1992), Beryllium isotope geochemistry in tropical river basins, *Geochim. Cosmochim. Acta*, *56*, 1607–1624.

Brown, L. (1987), ^{10}Be as a tracer of erosion and sediment transport, *Chem. Geol.*, *65*(3–4), 189–196, doi:10.1016/0168-9622(87)90002-9.

Brown, L., M. J. Pavich, R. E. Hickman, J. Klein, and R. Middleton (1988), Erosion of the eastern United States observed with ^{10}Be, *Earth Surf. Processes Landforms*, *13*(5), 441–457.

Chmeleff, J., F. von Blanckenburg, K. Kossert, and D. Jakob (2010), Determination of the ^{10}Be half-life by multicollector ICP-MS and liquid scintillation counting, *Nucl. Instrum. Methods Phys. Res., Sect. B*, *268*(2), 192–199.

Coe, M. T., M. H. Costa, A. Botta, and C. Birkett (2002), Long-term simulations of discharge and floods in the Amazon Basin, *J. Geophys. Res.*, *107*(D20), 8044, doi:10.1029/2001JD000740.

Dellinger, M., J. Gaillardet, J. Bouchez, D. Calmels, V. Galy, R. G. Hilton, P. Louvat, and C. France-Lanord (2014), Lithium isotopes in large rivers reveal the cannibalistic nature of modern continental weathering and erosion, *Earth Planet. Sci. Lett.*, *401*, 359–372, doi:10.1016/j.epsl.2014.05.061.

Dosseto, A., B. Bourdon, J. Gaillardet, C. J. Allegre, and N. Filizola (2006), Time scale and conditions of weathering under tropical climate: Study of the Amazon basin with U-series, *Geochim. Cosmochim. Acta*, *70*(1), 71–89, doi:10.1016/j.gca.2005.06.033.

Dunne, T., L. A. K. Mertes, R. H. Meade, J. E. Richey, and B. R. Forsberg (1998), Exchanges of sediment between the flood plain and channel of the Amazon River in Brazil, *Geol. Soc. Am. Bull.*, *110*(4), 450–467.

Edmond, J. M., M. R. Palmer, C. I. Measures, B. Grant, and R. F. Stallard (1995), The fluvial geochemistry and denudation rate of the Guyana Shield in Venezuela, Colombia, and Brazil, *Geochim. Cosmochim. Acta*, *59*(16), 3301–3325.

Espinoza Villar, J. C., J. Ronchail, J. L. Guyot, G. Cochonneau, N. Filizola, W. Lavado, E. De Oliveira, R. Pombosa, and P. Vauchel (2009), Spatio-temporal rainfall variability in the Amazon basin countries (Brazil, Peru, Bolivia, Colombia, and Ecuador), *Int. J. Climatol.*, *29*(11), 1574–1594.

Field, C. V., G. A. Schmidt, D. Koch, and C. Salyk (2006), Modeling production and climate-related impacts on Be-10 concentration in ice cores, *J. Geophys. Res.*, *111*, D15107, doi:10.1029/2005JD006410.
Filizola, N., F. Seyler, M. H. Mourao, W. Arruda, N. Spinola, and J. Guyot (2009), Study of the variability in suspended sediment discharge at Manacapuru, Amazon River, Brazil, *Latin Am. J. Sedimentol. Basin Anal.*, *16*(2), 93–99.
Foster, M. A., R. S. Anderson, C. E. Wyshnytzky, W. B. Ouimet, and D. P. Dethier (2015), Hillslope lowering rates and mobile-regolith residence times from in situ and meteoric ^{10}Be analysis, Boulder Creek Critical Zone Observatory, Colorado, *Geol. Soc. Am. Bull.*, doi:10.1130/b31115.1.
Frank, M., D. Porcelli, P. Andersson, M. Baskaran, G. Björk, P. W. Kubik, B. Hattendorf, and D. Guenther (2009), The dissolved Beryllium isotope composition of the Arctic Ocean, *Geochim. Cosmochim. Acta*, *73*(20), 6114–6133, doi:10.1016/j.gca.2009.07.010.
Gaillardet, J., B. Dupré, C. J. Allègre, and P. Negrel (1997), Chemical and physical denudation in the Amazon River basin, *Chem. Geol.*, *142*(3–4), 141–173.
Gaillardet, J., B. Dupré, and C. J. Allègre (1999), Geochemistry of large river suspended sediments: Silicate weathering or recycling tracer?, *Geochim. Cosmochim. Acta*, *63*(23–24), 4037–4051, doi:10.1016/s0016-7037(99)00307-5.
Graly, J. A., P. R. Bierman, L. J. Reusser, and M. J. Pavich (2010), Meteoric ^{10}Be in soil profiles: A global meta-analysis, *Geochim. Cosmochim. Acta*, *74*(23), 6814–6829, doi:10.1016/j.gca.2010.08.036.
Graly, J. A., L. J. Reusser, and P. R. Bierman (2011), Short and long-term delivery rates of meteoric ^{10}Be to terrestrial soils, *Earth Planet. Sci. Lett.*, *302*(3–4), 329–336, doi:10.1016/j.epsl.2010.12.020.
Granger, D. E., N. A. Lifton, and J. K. Willenbring (2013), A cosmic trip: 25 years of cosmogenic nuclides in geology, *Geol. Soc. Am. Bull.*, *125*(9–10), 1379–1402, doi:10.1130/b30774.1.
Gu, Z. Y., D. Lal, T. S. Liu, J. Southon, M. W. Caffee, Z. T. Guo, and M. Y. Chen (1996), Five million year ^{10}Be record in Chinese loess and red-clay: Climate and weathering relationships, *Earth Planet. Sci. Lett.*, *144*(1–2), 273–287, doi:10.1016/0012-821x(96)00156-2.
Guyot, J. L. (1993), Hydrogéochimie des fleuves de l'Amazonie Bolivienne, PhD thesis thesis, Bordeaux I, Bordeaux, France.
Guyot, J. L., N. Filizola, and A. Laraque (2005), The suspended sediment flux of the River Amazon at Obidos, Brazil, 1995–2003, paper presented at Proceedings of symposium S1 held during the Seventh IAHS Scientific Assembly, IAHS Publication, Foz do Iguaco, BRAZIL, Apr 03–09.
Guyot, J. L., N. Filizola, J. Quintanilla, and J. Cortez (1996), Dissolved solids and suspended sediment yields in the Rio Madeira basin, from the Bolivian Andes to the Amazon, paper presented at Proceedings of the Exeter Symposium, IAHS Publication, Exeter, U. K.
Haase, R. (1992), Physical and chemical properties of savanna soils in Northern Bolivia, *Catena*, *19*(1), 119–134, doi:10.1016/0341-8162(92)90020-c.
Heikkilä, U., and F. von Blanckenburg (2015), The global distribution of Holocene meteoric ^{10}Be fluxes from atmospheric models, Distribution maps for terrestrial Earths surface applications, GFZ Data Services, GFZ Potsdam, Germany, doi:10.5880/GFZ.3.4.2015.001.
Heikkilä, U., J. Beer, J. A. Abreu, and F. Steinhilber (2013a), On the atmospheric transport and deposition of the cosmogenic radionuclides (^{10}Be): A review, *Space Sci. Rev.*, *176*(1–4), 321–332, doi:10.1007/s11214-011-9838-0.
Heikkilä, U., S. J. Phipps, and A. M. Smith (2013b), Be-10 in late deglacial climate simulated by ECHAM5-HAM—Part 1: Climatological influences on Be-10 deposition, *Clim. Past*, *9*(6), 2641–2649, doi:10.5194/cp-9-2641-2013.
Jeandel, C. (1993), Concentration and isotopic composition of Nd in the South Atlantic Ocean, *Earth Planet. Sci. Lett.*, *117*(3–4), 581–591, doi:10.1016/0012-821X(93)90104-H.
Johnsson, M. J., R. F. Stallard, and N. Lundberg (1991), Controls on the composition of fluvial sands from a tropical weathering environment: Sands of the Orinoco River drainage basin, Venezuela and Colombia, *Geol. Soc. Am. Bull.*, *103*(12), 1622–1647, doi:10.1130/0016-7606(1991)103<1622:cotcof>2.3.co;2.
Korschinek, G., et al. (2010), A new value for the half-life of ^{10}Be by heavy-ion elastic recoil detection and liquid scintillation counting, *Nucl. Instrum. Methods Phys. Res., Sect. B*, *268*(2), 187–191.
Kubik, P. W., and M. Christl (2010), ^{10}Be and ^{26}Al measurements at the Zurich 6 MV Tandem AMS facility, *Nucl. Instrum. Methods Phys. Res., Sect. B*, *268*, 808–883, doi:10.1016/j.nimb.2009.10.054.
Kuehni, A., and O. A. Pfiffner (2001), The relief of the Swiss Alps and adjacent areas and its relation to lithology and structure: Topographic analysis from a 250-m DEM, *Geomorphology*, *41*(4), 285–307, doi:10.1016/s0169-555x(01)00060-5.
Laraque, A., N. Filizola, and J. L. Guyot (2005), The spatial and temporal variability of sediment transport in the Brazilian Amazon basin, based on a regular 10-day sampling programme, paper presented at Proceedings of symposium S1 held during the Seventh IAHS Scientific Assembly, IAHS Publication, Foz do Iguaco, BRAZIL, Apr 03–09.
Lauer, J. W., and J. K. Willenbring (2010), Steady-state reach-scale theory for radioactive tracer concentration in a simple channel/floodplain system, *J. Geophys. Res.*, *115*, F04018, doi:10.1029/2009JF001480.
Latrubesse, E. M. (2015), Large rivers, megafans and other Quaternary avulsive fluvial systems: A potential "who's who" in the geological record, *Earth Sci. Rev.*, *146*, 1–30, doi:10.1016/j.earscirev.2015.03.004.
Martinez, J. M., J. L. Guyot, N. Filizola, and F. Sondag (2009), Increase in suspended sediment discharge of the Amazon River assessed by monitoring network and satellite data, *Catena*, *79*(3), 257–264.
Masarik, J., and J. Beer (1999), Simulation of particle fluxes and cosmogenic nuclide production in the Earth's atmosphere, *J. Geophys. Res.*, *104*(D10), 12,099–12,111, doi:10.1029/1998JD200091.
Maurice, L., I. Quiroga, J. L. Guyot, and O. Malm (1999), Mercury pollution in the Upper Beni River, Amazonian Basin: Bolivia, *Ambio*, *28*(4), 302–306.
Meade, R. H., T. Dunne, J. E. Richey, U. Santos, and E. Salati (1985), Storage and remobilization of suspended sediment in the Lower Amazon River of Brazil, *Science*, *228*, 488–490.
Moquet, J.-S., et al. (2011), Chemical weathering and atmospheric/soil CO_2 uptake in the Andean and Foreland Amazon basins, *Chem. Geol.*, *287*, 1–26.
Moreira-Turcq, P., P. Seyler, J. L. Guyot, and H. Etcheber (2003), Exportation of organic carbon from the Amazon River and its main tribuatries, *Hydrol. Processes*, *17*, 1329–1344.
Ouimet, W., D. Dethier, P. Bierman, C. Wyshnytzky, N. Shea, and D. H. Rood (2015), Spatial and temporal variations in meteoric ^{10}Be inventories and long-term deposition rates, Colorado Front Range, *Quat. Sci. Rev.*, *109*, 1–12, doi:10.1016/j.quascirev.2014.11.003.
Schwertmann, U., J. Friedl, and H. Stanjek (1999), From Fe(III) ions to ferrihydrite and then to hematite, *J. Colloid Interface Sci.*, *209*(1), 215–223, doi:10.1006/jcis.1998.5899.
Shen, C., J. Beer, P. W. Kubik, M. Suter, M. Borkovec, and T. S. Liu (2004), Grain size distribution, ^{10}Be content and magnetic susceptibility of micrometer-nanometer loess materials, *Nucl. Instrum. Methods Phys. Res., Sect. B*, *223–224*, 613–617.
Silva, J. F., M. R. Fariñas, J. M. Felfili, and C. A. Klink (2006), Spatial heterogeneity, land use and conservation in the cerrado region of Brazil, *J. Biogeogr.*, *33*(3), 536–548, doi:10.1111/j.1365-2699.2005.01422.x.

Sioli, H. (1968), Hydrochemistry and geology in the Brazilian Amazon region, *Amazoniana*, *1*, 267–277.
Steinhilber, F., et al. (2012), 9,400 years of cosmic radiation and solar activity from ice cores and tree rings, *Proc. Natl. Acad. Sci. U.S.A.*, *109*(16), 5967–5971, doi:10.1073/pnas.1118965109.
Tessier, A., P. G. C. Campbell, and M. Bisson (1979), Sequential extraction procedure for the speciation of particulate trace metals, *Anal. Chem.*, *51*(7), 844–851, doi:10.1021/ac50043a017.
von Blanckenburg, F. (2005), The control mechanisms of erosion and weathering at basin scale from cosmogenic nuclides in river sediment, *Earth Planet. Sci. Lett.*, *237*(3–4), 462–479, doi:10.1016/j.epsl.2005.06.030.
von Blanckenburg, F., and J. Bouchez (2014), River fluxes to the sea from the ocean's $^{10}Be/^{9}Be$ ratio, *Earth Planet. Sci. Lett.*, *387*, 34–43, doi:10.1016/j.epsl.2013.11.004.
von Blanckenburg, F., J. Bouchez, and H. Wittmann (2012), Earth surface erosion and weathering from the ^{10}Be (meteoric)/^{9}Be ratio, *Earth Planet. Sci. Lett.*, *351–352*, 295–305.
von Blanckenburg, F., J. Bouchez, D. E. Ibarra, and K. Maher (2015), Stable runoff and weathering fluxes into the oceans over Quaternary climate cycles, *Nat. Geosci.*, *8*(7), 538–542, doi:10.1038/ngeo2452.
Waychunas, G. A., C. S. Kim, and J. F. Banfield (2005), Nanoparticulate iron oxide minerals in soils and sediments: Unique properties and contaminant scavenging mechanisms, *J. Nanopart. Res.*, *7*(4–5), 409–433, doi:10.1007/s11051-005-6931-x.
West, A. J., A. Galy, and M. Bickle (2005), Tectonic and climatic controls on silicate weathering, *Earth Planet. Sci. Lett.*, *235*(1–2), 211–228.
West, N., E. Kirby, P. Bierman, R. Slingerland, L. Ma, D. Rood, and S. Brantley (2013), Regolith production and transport at the Susquehanna Shale Hills Critical Zone Observatory, Part 2: Insights from meteoric ^{10}Be, *J. Geophys. Res. Earth Surf.*, *118*, 1877–1896, doi:10.1002/jgrf.20121.
Willenbring, J. K., and F. von Blanckenburg (2010), Meteoric cosmogenic Beryllium-10 adsorbed to river sediment and soil: Applications for Earth-surface dynamics, *Earth Sci. Rev.*, *98*(1–2), 105–122.
Wittmann, H., and F. von Blanckenburg (2009), Cosmogenic nuclide budgeting of floodplain sediment transfer, *Geomorphology*, *109*(3–4), 246–256, doi:10.1016/j.geomorph.2009.03.006.
Wittmann, H., F. von Blanckenburg, J. L. Guyot, L. Maurice, and P. W. Kubik (2009), From source to sink: Preserving the cosmogenic ^{10}Be-derived denudation rate signal of the Bolivian Andes in sediment of the Beni and Mamoré foreland basins, *Earth Planet. Sci. Lett.*, *288*(3–4), 463–474, doi:10.1016/j.epsl.2009.10.008.
Wittmann, H., F. von Blanckenburg, L. Maurice, J. L. Guyot, N. Filizola, and P. W. Kubik (2011a), Sediment production and delivery in the Amazon River basin quantified by in situ-produced cosmogenic nuclides and recent river loads, *Geol. Soc. Am. Bull.*, *123*(5–6), 934–950, doi:10.1130/B30317.1.
Wittmann, H., F. von Blanckenburg, L. Maurice, J.-L. Guyot, and P. Kubik (2011b), Recycling of Amazon floodplain sediment quantified by cosmogenic Al-26 and Be-10, *Geology*, *39*(5), 467–470.
Wittmann, H., F. von Blanckenburg, J. Bouchez, N. Dannhaus, R. Naumann, M. Christl, and J. Gaillardet (2012), The dependence of meteoric ^{10}Be concentrations on particle size in Amazon River bed sediment and the extraction of reactive $^{10}Be/^{9}Be$ ratios, *Chem. Geol.*, *318–319*, 126–138, doi:10.1016/j.chemgeo.2012.04.031.
You, C. F., T. Lee, L. Brown, J. J. Shen, and J. C. Chen (1988), ^{10}Be study of rapid erosion in Taiwan, *Geochim. Cosmochim. Acta*, *52*(11), 2687–2691, doi:10.1016/0016-7037(88)90037-3.
You, C.-F., T. Lee, and Y.-H. Li (1989), The partition of Be between soil and water, *Chem. Geol.*, *77*(2), 105–118.